J. Fluid Mech. (1987), *vol.* 182, *pp.* 335–368
Printed in Great Britain

Melt motion in a Czochralski crystal puller with an axial magnetic field: motion due to buoyancy and thermocapillarity

By L. N. HJELLMING AND J. S. WALKER

Department of Theoretical and Applied Mechanics, University of Illinois,
Urbana, IL 61801, USA

(Received 8 October 1986 and in revised form 7 March 1987)

In the Czochralski process a single crystal is grown from liquid in a crucible. An axial magnetic field suppresses turbulence in the melt and thus reduces the density of microdefects in the crystal. This paper treats the melt motion due to buoyancy and thermocapillarity. The magnitude of this motion decreases roughly like B^{-2}, as the magnetic field strength B is increased. The separate circulations due to buoyancy and thermocapillarity are roughly equal at an early stage of growing a crystal. However the circulation due to thermocapillarity is nearly independent of the melt depth, while that due to buoyancy is proportional to the square of the depth. Therefore as the crystal grows and the melt depth decreases, thermocapillarity becomes progressively more dominant. When the heat flux into the melt is used to define the characteristic temperature difference and velocity, the stream functions are rather insensitive to changes in the thermal boundary conditions at the free surface and at the crucible bottom, provided the overall heat balance of the system is correctly estimated. This is fortunate because there is considerable uncertainty about these boundary conditions. The exception to this insensitivity is that the melt motion due to thermocapillarity is sensitive to changes in the amount of heat lost through the part of the free surface adjacent to the crystal.

1. Introduction

In the Czochralski process a single crystal is grown from a melt contained in a crucible inside a furnace, as shown in figure 1. There are heaters around the crucible which prevent the solidification of the melt except at the crystal–melt interface. There are large radial temperature gradients in the melt, so that buoyancy and thermocapillarity drive melt motions. Under buoyancy hot fluid rises near the vertical crucible wall and flows inward along the free surface. As the fluid cools it descends and then returns near the crucible bottom to the vertical crucible wall. The surface tension decreases from the crystal to the hotter crucible, so that thermocapillarity drives an inward flow near the free surface with a return flow deeper in the melt.

Here we consider the magnetic Czochralski process with a uniform, axial magnetic field which is produced by a solenoid around the furnace. The magnetic field suppresses turbulence in the melt and the associated fluctuations in the heat flux across the crystal–melt interface. Because of these fluctuations, without a magnetic field the crystal alternately grows and remelts, which produces more microdefects in the crystal (Kuroda, Kozuka & Takano 1984). A crystal grown in a magnetic

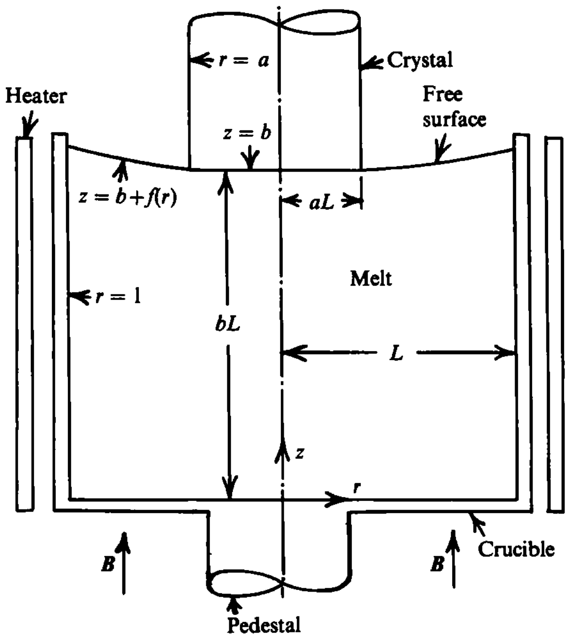

FIGURE 1. Czochralski crystal puller with a uniform, axial magnetic field $\boldsymbol{B}$.

Czochralski puller has a lower microdefect density. Previous treatments of melt motion in a magnetic Czochralski puller involve the numerical solution of the coupled Navier–Stokes equations (with buoyancy and the electromagnetic body force), the heat equation, Ohm's law and the conservation equations for mass and electric current (Langlois & Walker 1982). For the typical magnetic field strengths ($B = 0.1$–1.0 T), the inertial terms in the Navier–Stokes equations can be neglected everywhere and the viscous terms are only significant in the boundary layers and in a free-shear or interior layer lying along the vertical cylinder beneath the outer edge of the crystal. If we assume that the temperature $T(r, z)$ is given, then we can analytically solve all the equations, except the heat equation, for the velocity, pressure and electric current density in each inviscid core region, in each viscous boundary layer and in the free-shear layer. These simple analytical solutions in terms of the unknown temperature provide physical insights into the melt motion. In addition we can analytically solve the heat equation for the boundary and free-shear layers. The analytical solutions for the core velocities are introduced into the heat equation to obtain a nonlinear equation involving a single unknown, $T(r, z)$. This scalar equation is solved numerically for the inner core region beneath the crystal and for the outer core region beneath the free surface. We discuss the variations of the melt motion with changes in the thermal boundary conditions at the free surface and at the crucible bottom, with changes in the melt depth during the growth of a crystal, and with changes in the magnetic field strength. For a typical Czochralski process, the convective heat transfer can be ignored for $B \geqslant 0.46T$, so that the temperature for simple thermal conduction through the melt can be used to determine the melt motion due to buoyancy and thermocapillarity.

In §2, we formulate the problem, present the assumptions and discuss the boundary conditions. In §§3 and 4, we present the separate solutions for the melt motion due to buoyancy and thermocapillarity, respectively. In §§5 and 6, we discuss the combined motions for various depths and for various magnetic field strengths, respectively. In §§3, 4 and 5, the buoyant and thermocapillary convections, and their variation with depth, are illustrated with the temperature field for pure conduction, which is the correct temperature field for a sufficiently strong magnetic field. In §6, we include the convective heat transfer and solve the nonlinear heat equation to obtain the temperature field for modest magnetic field strengths and the resulting melt motions. In §7, we discuss the superposition of the melt motion associated with the rotation of the crucible and crystal and with the crystal growth. In §8, we discuss the heat transfer from the melt to the crystal, we compare the present predictions to previous numerical results and we discuss certain implications for the mass transport of oxygen and of dopants.

2. Problem formulation

With the Boussinesq approximation, the melt density is a linear function of the temperature in the gravitational body force and is a constant elsewhere. We assume that the surface tension is also a linear function of the temperature and that all other physical properties are constants. There is a uniform axial magnetic field $B\hat{z}$, where $\hat{z}$ is a vertical unit vector. The system is taken to be axisymmetric, so that the dependent variables and boundary conditions do not depend on the azimuthal coordinate θ.

In a typical Czochralski crystal puller, the melt depth decreases at a rate of 4×10^{-6} m/s, so that the melt motion is essentially steady at each depth. Without a magnetic field, the melt motion is frequently periodic, even for steady boundary conditions (Langlois 1981). As the magnetic field strength B increases from zero, first the mean flow becomes steady, secondly the turbulence disappears and finally all velocities are so small that inertial accelerations are negligible. We assume that B is sufficiently large that all three of these magnetic-field effects occur. The minimum values of B for the first two effects appear to be between 0.05 and 0.1 T, while the minimum value of B for the third effect appears to be between 0.1 and 0.2 T for a typical Czochralski puller. Hjellming & Walker (1986) treat the melt motions associated with the rotations of the crystal and crucible, but ignore the thermally driven motions. Here we treat buoyant and thermocapillary convections without rotation of the crystal or crucible. With our strong-magnetic-field assumption, all melt velocities are very small and the nonlinear inertial terms in the Navier–Stokes equations are negligible. Hence the melt motions due to buoyancy, thermocapillarity and centrifugal pumping can be treated independently and can then simply be superposed. Centrifugal pumping might still affect the buoyant and thermocapillary convections through its effects on the temperature. The principal components of the centrifugally driven flow are radial jets near the crystal face and crucible bottom and a strong, axially elongated vortex beneath the crystal edge. In §7, we show that these motions have a negligible effect on the temperature for modest rotation rates (say, 15 to 20 r.p.m.) and for $B \geqslant 0.2$ T, so that the present solutions and those presented by Hjellming & Walker (1986) can be superposed with no interaction.

For the present axisymmetric motion without rotation of the crucible or crystal, $v_\theta = j_r = j_z = \phi = 0$, where $\boldsymbol{v}, \boldsymbol{j}$ and ϕ are the velocity, electric current density and electric potential function, respectively. Hjellming & Walker (1986) show that the meridional motion (v_r, v_z) due to centrifugal pumping depends critically on the relatively small electrical conductivity of the crystal. This dependence arises because (i) the electric potential ϕ depends on the division of the meridional current (j_r, j_z)

between the crystal and the crystal-face boundary layer, (ii) the azimuthal velocity v_θ equals the radial derivative of ϕ, and (iii) the centrifugal force, v_θ^2/r, drives the meridional motion. For the present problem, $v_\theta = 0$ in both the melt and the crystal, so that $\phi = j_r = j_z = 0$ everywhere. With a purely meridional motion, the induced electric field $\boldsymbol{v} \times \boldsymbol{B}$ cannot produce an electric potential gradient because v_z is parallel to $\boldsymbol{B}$ and the axisymmetry precludes an azimuthal electric field due to v_r. Therefore, the electrical conductivity of the crystal has no effect on the thermocapillary and buoyant convections once B is large enough to decouple the centrifugal pumping.

We assume that the magnetic Reynolds number

$$R_\mathrm{m} = \mu\sigma UL \ll 1,$$

so that we can neglect the magnetic field produced by the electric currents in the melt and in the crystal. The characteristic length L is the inside radius of the crucible and the characteristic velocity is

$$U = \frac{\rho g\alpha(\Delta T)}{\sigma B^2}. \tag{1}$$

The melt's physical constants are the magnetic permeability μ ($4\pi \times 10^{-7}$ H/m), the electrical conductivity σ (10^6 S/m), the density ρ at the melting temperature (2330 kg/m^3 at $T_\mathrm{s} = 1685$ K) and the volumetric expansion coefficient α (1.41×10^{-5}/K). All parameter values are based on the growth of a 7.6 cm diameter silicon crystal in a crucible with a 19 cm inside diameter ($L = 9.5$ cm and $a = 0.4$ in figure 1). The published values for some of the physical constants of molten silicon near its melting temperature vary by as much as a factor of ten. Here we consider changes in the melt motion due to changes in certain thermal boundary conditions or due to changes in the instantaneous depth bL or due to changes in the strength B of the uniform, axial magnetic field. We only consider one value for each of the physical constants of silicon and these values are given in parentheses. A future paper (Hjellming & Walker 1987) will treat the variations of the melt motion over the wide range of published values for the physical constants of silicon. The characteristic temperature difference (ΔT) is defined later. In order to estimate the values of the key parameters, we take $(\Delta T) = 100$ K, which is approximately the temperature difference between the crystal and the crucible at the free surface.

The dimensionless governing equations are

$$N^{-1}\mathrm{D}v_r = -\frac{\partial p}{\partial r} + j_\theta + M^{-2}\left(\nabla^2 v_r - \frac{v_r}{r^2}\right), \tag{2a}$$

$$N^{-1}\mathrm{D}v_z = -\frac{\partial p}{\partial z} + T + M^{-2}\nabla^2 v_z, \quad j_\theta = -v_r, \tag{2b,c}$$

$$\frac{\partial v_r}{\partial r} + \frac{v_r}{r} + \frac{\partial v_z}{\partial z} = 0, \quad Pe\mathrm{D}T = \nabla^2 T, \tag{2d,e}$$

where
$$\mathrm{D} = v_r\frac{\partial}{\partial r} + v_z\frac{\partial}{\partial z}, \quad \nabla^2 = \frac{\partial^2}{\partial r^2} + \frac{1}{r}\frac{\partial}{\partial r} + \frac{\partial^2}{\partial z^2}.$$

The coordinates (r, z) are normalized by L; the radial and axial melt velocities v_r and v_z are normalized by U; the azimuthal electric current density j_θ is normalized by $\sigma UB = \rho g\alpha(\Delta T)/B$; the dimensional temperature and gauge pressure (denoted by asterisks) are given by

$$T^* = T_\mathrm{s} + (\Delta T)\,T, \quad p^* = \rho gL(b-z) + \rho g\alpha(\Delta T)\,Lp. \tag{3a,b}$$

B (T)	U(mm/s)	R_m	N	M	Pe
0.1	3.22	3.8×10^{-4}	1.27×10^{2}	359	10.64
0.2	0.805	9.6×10^{-5}	2.03×10^{3}	719	2.66
0.3	0.358	4.3×10^{-5}	1.03×10^{4}	1078	1.18
0.4	0.201	2.4×10^{-5}	3.24×10^{4}	1437	0.665
0.6	0.089	1.1×10^{-5}	1.64×10^{5}	2156	0.295
0.8	0.050	6.0×10^{-6}	5.19×10^{5}	2875	0.166
1.0	0.032	3.8×10^{-6}	1.27×10^{6}	3593	0.106

TABLE 1. Values of the characteristic velocity and some parameters for a typical Czochralski silicon-crystal puller and for various magnetic field strengths B

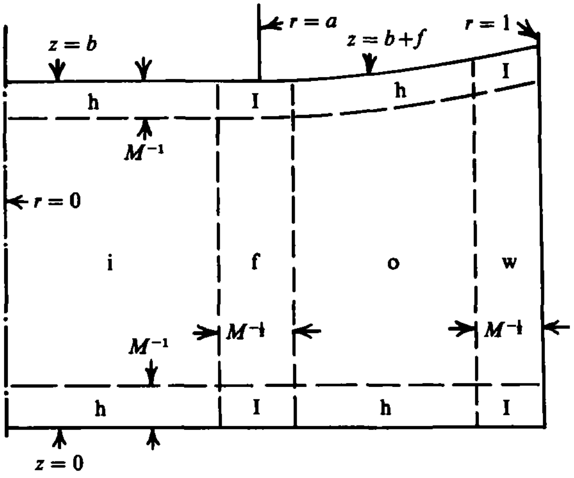

FIGURE 2. Meridional section showing subregions of the melt for $M \gg 1$.

The interaction parameter N, Hartmann number M and Péclet number Pe are defined by

$$N=\frac{\sigma B^2L}{\rho U}=\frac{\sigma^2B^4L}{\rho^2g\alpha(\Delta T)},\quad M=BL\left(\frac{\sigma}{\rho\nu}\right)^{\frac{1}{2}},$$

$$Pe=\frac{\rho c_h UL}{k}=\frac{\rho^2c_h g\alpha(\Delta T)L}{k\sigma B^2}.$$

The additional physical parameters for the melt that are introduced above are the kinematic viscosity ν (3×10^{-7} m^2/s), the specific heat c_h (10^3 J/kg K) and the thermal conductivity k (67 W/m K). The values of U, R_m, N, M and Pe for $B = 0.1$–1.0 T are given in table 1.

We assume that N is sufficiently large that the inertial terms on the left-hand sides of ($2a,b$) are negligible everywhere. We also assume the $M \gg 1$, so that M^{-1} is the small parameter in the asymptotic expansions for the flow variables in certain subregions of the melt. The subregions (shown in figure 2) are the outer (o) and inner (i) inviscid cores with $O(1)$ radial and axial derivatives, the Hartmann layers (h) with $O(M^{-1})$ thickness, the free-shear or interior layer (f) at $r = a$ with $O(M^{-\frac{1}{2}})$ thickness, the vertical wall layer (w) with $O(M^{-\frac{1}{2}})$ thickness and the intersection regions (I) with $O(M^{-\frac{1}{2}})\times O(M^{-1})$ dimensions. In §8, we conclude that the minimum value of B for the neglect of inertial effects and for the subdivision of the melt into these inviscid cores and viscous layers is between 0.1 and 0.2 T for a typical Czochralski puller with silicon. A variable with a subscript i, o, f, etc. denotes the leading term in the asymptotic expansion for that variable in the inner core, outer core, free-shear layer, etc.

The boundary conditions at the crystal face are

$$v_r = v_z = T = 0, \quad \text{at } z = b, \quad \text{for } 0 \leqslant r \leqslant a. \qquad (4a\text{–}c)$$

The dimensionless displacement $f(r)$ of the free surface from the horizontal plane $z = b$ is determined by the condition that the jump in pressure across the free surface is proportional to the local surface tension times the local curvature of the surface. Buoyancy and thermocapillarity produce a p of $O(1)$, which is the dimensionless deviation from a hydrostatic pressure. When we apply the jump condition to the gauge pressure (3*b*) at $z = b+f$, the resultant ordinary differential equation governing f indicates that f is comparable with $\alpha(\Delta T) = 0.00141$. To be consistent with the Boussinesq approximation, we neglect f and apply the other free-surface boundary conditions at $z = b$. The velocity boundary conditions at the free surface are

$$v_z = 0, \quad \frac{\partial v_r}{\partial z} = -M^2 Q \frac{\partial T}{\partial r} \quad \text{at } z = b \quad \text{for } a \leqslant r \leqslant 1, \qquad (5a, b)$$

where

$$Q = -\frac{\mathrm{d}\gamma/\mathrm{d}T^*}{\rho g \alpha L^2} = 0.036$$

and $\mathrm{d}\gamma/\mathrm{d}T^*$ (-1.04×10^{-4} N/m K) is the constant derivative of the surface tension γ with respect to the dimensional temperature T^*. The parameter Q equals the Marangoni number divided by the product of the Grashof and Prandtl numbers. It will turn out to be the ratio of a characteristic outer-core velocity due to thermocapillarity, namely

$$\frac{(-\mathrm{d}\gamma/\mathrm{d}T^*)(\Delta T)}{\sigma B^2 L^2},$$

to U. Published values of α and $\mathrm{d}\gamma/\mathrm{d}T^*$ for molten silicon near T_s range from the values used here to values that are ten and four times larger, respectively. Therefore Q can range from 0.0036 to 0.14, i.e. from 0.1 to 4 times the value used here. In the present inertialess approximation, the buoyant and thermocapillary convections are treated separately and are simply superposed. If α is increased by a factor of ten, then the present thermocapillary stream-function values are multiplied by 0.1 before being added to the buoyant stream-function values. If $\mathrm{d}\gamma/\mathrm{d}T^*$ is increased by a factor of four, then the thermocapillary values are multiplied by four before this addition. This correction is exact for $Pe \ll 1$ and approximate for the other values of Pe considered here. We present separate key values of the buoyant and thermocapillary stream functions for each flow situation. Addition of these key values with a factor from 0.1 to 4 gives some concept of the effects of varying the values of α and $\mathrm{d}\gamma/\mathrm{d}T^*$. These variations are considered in detail by Hjellming & Walker (1987), and here we only consider the superposition for one pair of values for α and $\mathrm{d}\gamma/\mathrm{d}T^*$. These are the values used by Langlois (1981), Langlois & Walker (1982), and Langlois & Lee (1983*a*). These are also the values used by Langlois & Lee (1983*b*) for their 'low-buoyancy' case, and they present numerical results for melt motions without rotation of the crystal or crucible. In §8 we compare their numerical results with the present predictions, and we discuss their 'high-buoyancy' results to illustrate the effect of multiplying α by ten.

The heat conduction to the low-pressure argon cover gas is generally considered to be much smaller than the radiation from the free surface for molten silicon. The Stefan–Boltzmann radiation equation gives a local heat flux that is proportional to $[(T^*)^4-T_e^4]$, where T_e is the effective background temperature. We introduce the dimensionless temperature (3*a*), and neglect terms that are comparable with $(\Delta T)^2/T_s^2 = 0.0035$, so that the radiation equation becomes

$$\frac{\partial T}{\partial z} = -C_0 - C_1 T \quad \text{at } z = b \quad \text{for } a \leqslant r \leqslant 1. \tag{6}$$

Here $$C_0 = \frac{\epsilon\sigma_r L(T_s^4 - T_e^4)}{k(\Delta T)}, \quad C_1 = 4L\epsilon\sigma_r T_s^3 k^{-1} = 0.496,$$

σ_r (5.75×10^{-8} W/m^2 K^4) is the Stefan–Boltzmann radiation constant and ϵ (0.318) is the melt emissivity. All five terms from $(T^*)^4$ can be kept (Langlois 1981), but we have chosen to keep only the first two terms because (ΔT) is much smaller than T_s. The effective background temperature T_e depends on the temperatures, emissivities and geometries of the crystal, the unwetted crucible wall and the enclosing furnace wall, as well as the reflected radiation returning to the free surface. A complete calculation of T_e at each radial position on the free surface involves a complex numerical analysis. In most treatments of the radiation problem for the crystal, melt, unwetted crucible wall and furnace wall, either the melt is treated as an isothermal surface (Ramachandran & Dudukovic 1985) or as a rigid thermal conductor (Srivastava, Ramachandran & Dudukovic 1985). In either case, the melt motion is ignored in treating the radiation problem. On the other hand, mot previous treatments of the melt motion avoid the radiation problem by assuming some constant value for T_e. Assumed values range from $T_e = 0$ (Langlois 1981) to $T_e = T_s = 1685$ K (Langlois & Lee 1983*a*). In a recent paper, Langlois & Kim (1987) treat both the melt motion and a simplified radiation problem numerically. Here we treat the radiation problem in two steps. First we consider the melt motion due to buoyancy and due to thermocapillarity for three different constant values of T_e: 1685 K ($C_0 = 0$), 1574 K ($C_0 = 0.5$) and 1432 K ($C_0 = 1$). The results in §3 show that the dimensionless stream function for the buoyant convection is relatively insensitive to these changes in T_e. The results in §4 show that the dimensionless stream function for the thermocapillary convection is relatively insensitive to these changes in T_e for $0.5 < r < 1$, but is quite sensitive to these changes near the crystal edge, $0.4 < r < 0.5$. The rate of radiant heat loss from the free-surface element adjacent to the crystal edge strongly influences the local temperature gradient, which in turn controls the local thermocapillary convection. In our second step, we model the radiation balance for the free-surface element adjacent to the crystal and develop an analytical expression for T_e for this element as a function of temperatures, geometric parameters and melt depth. As the crystal grows, this free-surface element sees less of the cold furnace wall and more of the hot unwetted crucible wall, so that T_e increases.

The vertical d.c. heaters surrounding the crucible provide the heat input that balances the heat conduction to the crystal, the radiation from the free surface and any heat transfer through the crucible bottom. The appropriate thermal boundary condition at the vertical crucible wall is to prescribe the heat input here. This heat input probably varies with z, but there do not appear to be any published data to estimate this vertical variation. Therefore we take the heat flux q into the melt at

$r = 1$ to be a constant. We define $(\Delta T) = qL/k$, so that the boundary conditions at the vertical crucible wall are

$$v_r = v_z = 0, \quad \frac{\partial T}{\partial r} = 1 \quad \text{at } r = 1. \tag{7a–c}$$

There also do not appear to be any published data on the magnitude of the heat input. The electric current to the heaters is adjusted to prevent flaring, which is the solidification of the free surface adjacent to the crystal, and this appears to require a temperature difference of approximately 100 K between the crystal and the crucible at the free surface. For each solution presented here, we could obtain a situation-specific (ΔT) from the ratio of 100 K to the value of T at $r = 1$ and $z = b$. This would give situation-specific values for U, the parameters in table 1, C_0, etc. However, it turns out that T at $r = 1$ and $z = b$ is generally not too different from one, so that $(\Delta T) = 100$ K and $q = 70.5$ kW/m^2 give reasonable estimates of the orders of magnitude of the parameters.

During the first few hours of pulling a crystal, the heater projects only a short distance beyond the bottom of the crucible. Therefore the bottom receives little radiation from the heater, and this small heat input is concentrated near $r = 1$. Heat is lost through the bottom by radiation from the exposed part and by conduction down the pedestal (figure 1). Therefore, when b is relatively large, there is a heat loss through the bottom, and the heat flux varies from a maximum at $r = 0$ to a smaller value at $r = 1$. As the crystal is pulled, the crucible is raised so that the free surface remains in the same horizontal plane and progressively more of the heater extends beyond the bottom of the crucible. Heat input to the bottom overwhelms the heat loss, particularly near $r = 1$. Radiation to the pedestal increases its temperature and decreases the heat conduction from the crucible near $r = 0$. Therefore, when b is relatively small, there is a heat input through the bottom and the heat flux varies from a maximum at $r = 1$ to a smaller value at $r = 0$. To represent this situation, we use the boundary conditions

$$v_r = v_z = 0, \quad \frac{\partial T}{\partial z} = -D_0 - D_1 r^2 \quad \text{at } z = 0. \tag{8a–c}$$

We consider three values of b to model three progressive stages in the growth of a single crystal. For an early stage, $b = 1$ and we take $D_1 = -D_0 = 0.25$. The heat flux out of the bottom varies parabolically from $0.25q$ at $r = 0$ to zero at $r = 1$. For an intermediate stage, $b = 0.5$ and we take $D_0 = 0$, $D_1 = 0.25$. The heat flux into the bottom varies parabolically from zero at $r = 0$ to $0.25q$ at $r = 1$. For a final stage, $b = 0.25$ and we take $D_0 = 0$, $D_1 = 0.5$. Each heat flux into the bottom is double that for $b = 0.5$. Since there is only qualitative justification for these values of D_0 and D_1, the sensitivity of the melt motion to changes in D_0 and D_1 is important. The final boundary conditions

$$rv_r \rightarrow 0, \quad r\frac{\partial T}{\partial r} \rightarrow 0 \quad \text{at } r \rightarrow 0, \tag{9a, b}$$

exclude mass and heat sources at $r = 0$.

The equations (2*a–d*) (without the inertial terms) and the boundary conditions (4*a, b*), (5), (7*a, b*), (8*a, b*), (9*a*) represent a linear boundary-value problem governing p, v_r, v_z and j_θ for a given temperature $T(r, z)$. The velocities due to buoyancy and thermocapillarity are determined separately in terms of $T(r, z)$. The sum of the separate velocities is introduced into (2*e*) to obtain a nonlinear equation governing the temperature alone. The solutions for the velocities due to buoyancy and thermocapillarity are presented in §§3 and 4, respectively. In each case, the characteristics of the separate melt motions are illustrated using the temperature field for $Pe \ll 1$. This reference temperature is determined by solving $\nabla^2 T = 0$ with the boundary conditions (4*c*), (6), (7*c*), (8*c*), (9*b*). This simple potential problem was solved analytically using the separation-of-variables method, and numerically using an over-relaxed finite-difference method. The separation of variables leads to infinite series with convergence problems because the boundary conditions (4*c*), (6) lead to the representation of the Heaviside function $H(r-a)$ in terms of an infinite series of Bessel functions. This difficulty is overcome by subtracting out this jump at the crystal edge, but this step complicates the other boundary conditions. On the other hand, the finite-difference solution converges rapidly and accurately, and we use the numerical results to illustrate the implications of the analytical solutions for the melt velocities.

In §§3 and 4 we consider the motion due to buoyancy and thermocapillarity for arbitrary Pe and we investigate the sensitivity of each motion to changes in C_0, D_0 and D_1. In §5, we consider the combination of both flows for $Pe \ll 1$, and we investigate the variation of the melt motion with changes in depth. In §6, we consider the combined motion for finite Pe.

3. Melt motion due to buoyancy

To consider the buoyancy-driven motion separately, we set $Q = 0$ in the boundary condition (5*b*). For this case, there is no free-shear layer at $r = a$ and the two inviscid cores are combined into a single core denoted by the subscript c. The Hartmann layers match any radial velocity at $z = 0$ or b and satisfy the boundary conditions (4*a*), (5*b*), (8*a*). Assuming that Pe is at most $O(1)$, the jumps in v_z, T and $\partial T/\partial z$ are $O(M^{-1})$, $O(M^{-2})$ and $O(M^{-1})$, respectively, across the Hartmann layers on the crucible bottom and on the crystal face, but these jumps are $O(M^{-2})$, $O(M^{-3})$ and $O(M^{-2})$, respectively, across the Hartmann layer adjacent to the free surface.

The $O(1)$ core pressure, velocities and azimuthal electric-current density satisfy the equations (2*a*–*d*) without the inertial or viscous terms and satisfy the boundary conditions (4*b*), (5*a*), (8*b*), (9*a*). The solution is

$$v_{rc} = -j_{\theta c} = \frac{1}{r}\frac{\partial \psi_c}{\partial z}, \quad v_{zc} = -\frac{1}{r}\frac{\partial \psi_c}{\partial r}, \tag{10a,b}$$

$$\psi_c = rz\int_0^b \left(1-\frac{z^*}{b}\right)\frac{\partial T_c}{\partial r}(r,z^*)\,\mathrm{d}z^* - r\int_0^z (z-z^*)\frac{\partial T_c}{\partial r}(r,z^*)\,\mathrm{d}z^*, \tag{10c}$$

$$p_c = b^{-1}\int_0^b z^*[T_c(r,z^*)-T_c(a,z^*)]\,\mathrm{d}z^* - \int_z^b T_c(r,z^*)\,\mathrm{d}z^*. \tag{10d}$$

The displacement $f(r)$ of the free surface due to buoyancy is given by $\alpha(\Delta T)$ times (10*d*) evaluated at $z = b$. As far as the buoyancy-driven melt motion is concerned, the $O(1)$ core temperature $T_c(r,z)$ satisfies the boundary conditions (4*c*), (6), (8*c*), (9*b*).

Since $\partial T_c/\partial r$ is certainly not zero at $r = 1$, (10*a*, *c*) indicate that v_{rc} is not zero at $r = 1$. Therefore some of the $O(1)$ flow enters the vertical wall layer at some elevations and leaves at other elevations. An $O(M^{\frac{1}{2}})$ axial velocity inside this layer is required to accomplish this vertical redistribution of the $O(1)$ flow. We stretch the radial coordinate by introducing $r = 1 + M^{-\frac{1}{2}}R$. Inside this layer v_r and j_θ are $O(1)$, v_z is $O(M^{\frac{1}{2}})$,

$$p = p_{\mathrm{c}}(1, z) + M^{-\frac{1}{2}} p_{\mathrm{w}}(R, z)$$

and T is given by an identical expression with each p replaced by T. For $Pe = O(1)$, the equations (2*a*–*e*) give

$$v_{r\mathrm{w}} = -j_{\theta\mathrm{w}} = -\frac{\partial p_{\mathrm{w}}}{\partial R} = \frac{\partial \psi_{\mathrm{w}}}{\partial z}, \quad v_{z\mathrm{w}} = -\frac{\partial \psi_{\mathrm{w}}}{\partial R}, \tag{11a, b}$$

$$\frac{\partial p_{\mathrm{w}}}{\partial z} = T_{\mathrm{w}} - \frac{\partial^3 \psi_{\mathrm{w}}}{\partial R^3}, \quad \frac{\partial^2 T_{\mathrm{w}}}{\partial R^2} = -Pe \frac{\partial T_{\mathrm{c}}}{\partial z}(1, z) \frac{\partial \psi_{\mathrm{w}}}{\partial R}, \tag{11c, d}$$

where $\psi_{\mathrm{w}}(R, z)$ is the vertical-wall-layer stream function. The boundary conditions (7) become

$$\psi_{\mathrm{w}} = \frac{\partial \psi_{\mathrm{w}}}{\partial R} = 0, \quad \frac{\partial T_{\mathrm{w}}}{\partial R} = 1 \quad \text{at } R = 0. \tag{12a–c}$$

Matching the core solution (10) gives the boundary conditions

$$\psi_{\mathrm{w}} \to \psi_{\mathrm{c}}(1, z), \quad \frac{\partial T_{\mathrm{w}}}{\partial R} \to \frac{\partial T_{\mathrm{c}}}{\partial r}(1, z), \quad \text{as } R \to -\infty. \tag{13a, b}$$

Like the Hartmann layers, the intersection regions (I) match any radial velocity in the vertical wall layer, but the conditions (5*a*), (8*b*) hold for all R, so that

$$\psi_{\mathrm{w}} = 0 \quad \text{at } z = 0 \text{ and } b. \tag{14}$$

Equation (11*d*) is integrated once with respect to R and the boundary conditions (12*a*, *c*) are used to determine the integration function of z. The result is

$$\frac{\partial T_{\mathrm{w}}}{\partial R} = 1 - Pe \frac{\partial T_{\mathrm{c}}}{\partial z}(1, z)\, \psi_{\mathrm{w}}. \tag{15}$$

The matching conditions (13) now give

$$\frac{\partial T_{\mathrm{c}}}{\partial r}(1, z) = 1 - Pe\, \psi_{\mathrm{c}}(1, z) \frac{\partial T_{\mathrm{c}}}{\partial z}(1, z) \tag{16}$$

for the jump in the $O(1)$ radial heat flux across the vertical wall layer. Since $\psi_{\mathrm{c}}(1, z) > 0$, there is upward flow in this wall layer. If $\partial T_{\mathrm{c}}/\partial z > 0$, then the rising fluid is getting hotter and is absorbing some of the heat flux from the vertical crucible wall before the heat reaches the core. If $\partial T_{\mathrm{c}}/\partial z < 0$, then the rising fluid is getting colder and the core receives the heat input from the heater plus the heat rejected by the rising fluid.

Equations (11*a*, *c*), (15) are combined to obtain an equation governing ψ_{w}:

$$\frac{\partial^2 \psi_{\mathrm{w}}}{\partial z^2} = \frac{\partial^4 \psi_{\mathrm{w}}}{\partial R^4} + Pe \frac{\partial T_{\mathrm{c}}}{\partial z}(1, z)\, \psi_{\mathrm{w}} - 1. \tag{17}$$

Equation (17) and the boundary conditions (12*a*, *b*), (13*a*), (14) constitute a well-posed boundary-value problem governing $\psi_{\mathrm{w}}(R, z)$, assuming that $\partial T_{\mathrm{c}}/\partial z$, at $r = 1$, is known. This problem is solved by introducing the Fourier cosine transform with respect to R of $[\psi_{\mathrm{w}}(R, z) - \psi_{\mathrm{c}}(1, z)]$. This incorporates the boundary conditions (12*b*), (13*a*) and introduces the unknown function $F(z) = \partial^3 \psi_{\mathrm{w}}/\partial R^3$, evaluated at $R = 0$. Equation (17) is reduced to an ordinary differential equation in z with a variable coefficient and with an inhomogeneous term involving F. The conditions (14) show that the transformed variable is zero at $z = 0$ and b. The solution is introduced into the Fourier inversion formula to obtain an expression for ψ_w in terms of $F(z)$. This expression is introduced into the remaining boundary condition (12*a*) to obtain a singular integral equation governing $F(z)$. This integral equation generally requires a numerical solution (Walker, Ludford & Hunt 1971) unless $\partial T_c/\partial z$ can be approximated by a very simple function, e.g. a constant. Once F is determined analytically or numerically, the expression for ψ_w is introduced into (11*a*, *b*), (15) in order to obtain v_{rw}, v_{zw}, $j_{\theta w}$, p_w and T_w. Velocity profiles are not presented here. For the present problem, only two aspects of the vertical wall layer are important: (i) the jump in the radial heat flux across this layer, which is given by (16) in term of core variables only, and (ii) the fact that this layer matches any $v_c(1,z)$ given by (10*a*, *c*) and provides whatever vertical flow is needed to complete the streamlines inside this layer. The velocity distribution inside the vertical wall layer is important for the mass transport of the oxygen entering the melt from the vertical crucible wall. Vertical-wall-layer velocity profiles will be presented in a future paper treating the mass transport associated with the present melt motions.

The sensitivity of the core solution (10) to changes in the coefficients C_0, D_0 and D_1 in the thermal boundary conditions (6), (8*c*) can be illustrated with a single pair of values for Pe and b. In this section we use $Pe \ll 1$, corresponding to a strong magnetic field, and $b = 1$, corresponding to an early stage in the growth of a crystal. Actually we use $b = 0.9875$ because of the finite-difference grid. For $Pe \ll 1$, the boundary condition (16) reduces to the original wall condition (7*c*).

The streamlines for $C_0 = 0$ ($T_e = T_s = 1685$ K) and $D_1 = -D_0 = 0.25$ are shown in figure 3. Part of the streamline for $\psi_c = 0.001$ is shown as a dashed line to illustrate that the fluid near $r = 0$ is nearly quiescent. The streamlines for $C_0 = D_0 = D_1 = 0$ (thermally insulating crucible bottom) are virtually identical with those shown in figure 3. Similarly the streamlines for $D_1 = -D_0 = 0.25$ and for $C_0 = 0.5$ ($T_e = 1574$ K) or for $C_0 = 1.0$ ($T_e = 1432$ K) are almost indistinguishable from those shown in figure 3. One reason for this insensitivity is the choice of (ΔT) which leads to the boundary condition (7*c*). For $Pe \ll 1$, this boundary condition and the solution (10*c*) give

$$\psi_c(1,z) = \tfrac{1}{2}z(b-z), \tag{18}$$

so that the maximum value of ψ_c is $0.125b^2$ at $r = 1$ and $z = 0.5b$. The amount and vertical distribution of the buoyancy-driven circulation is primarily determined by the values (18) which are independent of C_0, D_0 and D_1. For finite Pe, the boundary condition (16) leads to larger or smaller values of $\psi_c(1,z)$ than those given by (18) because of the heat rejected or absorbed by the vertical wall layer. Nevertheless, these values at $r = 1$ are still insensitive to changes in C_0, D_0 and D_1 and are the dominant values of ψ_c for the entire melt. The second reason for the insensitivity of the solution (10) to changes in these coefficients is that the integrals in (10*c*) appear to smooth out the effects of local changes of $\partial T_c/\partial r$.

While the streamlines based on (10*c*) do not change significantly, the values of the temperature do, as illustrated by the values of T at the free surface shown in figure 4. If we are actually prescribing q, the (ΔT) is known and the actual melt motion is insensitive to changes in C_0, D_0 and D_1. On the other hand, if we are prescribing the temperature difference between the crystal and the crucible at the free surface, say 100 K, then the values of (ΔT), q, U and the dimensionless parameters depend on C_0, D_0 and D_1. For cases (*a*), (*b*), (*c*) and (*d*) in figure 4, $(\Delta T) = 53.4$, 56.8, 73.4 and 104.2 K, respectively. The values of U, R_m, N and Pe in table 1 assumed that $(\Delta T) = 100$ K, so that these values are changed appropriately. Therefore if we are prescribing the free-surface temperature difference in order to prevent flaring, the

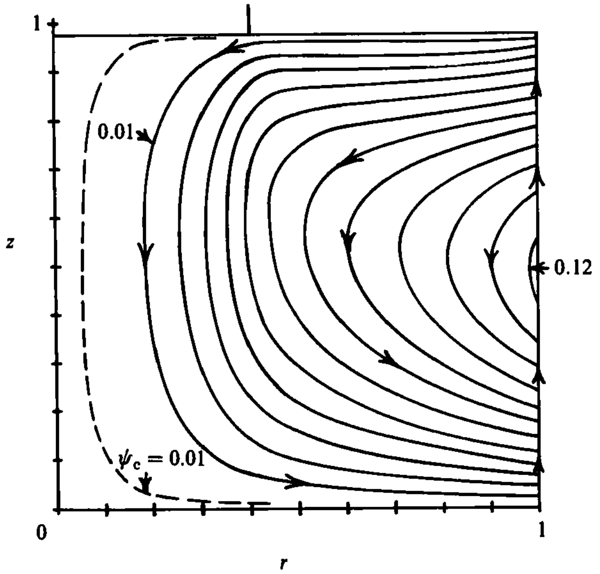

FIGURE 3. Streamlines for buoyancy only and with $Pe \ll 1$, $b = 0.9875$, $C_0 = 0$, $D_1 = -D_0 = 0.25$, and $\psi_c = 0.01m$, for $m = 1$–12. Part of the streamline $\psi_c = 0.001$ is shown as a dashed line. The upward flow in the vertical wall layer is represented by the line at $r = 1$.

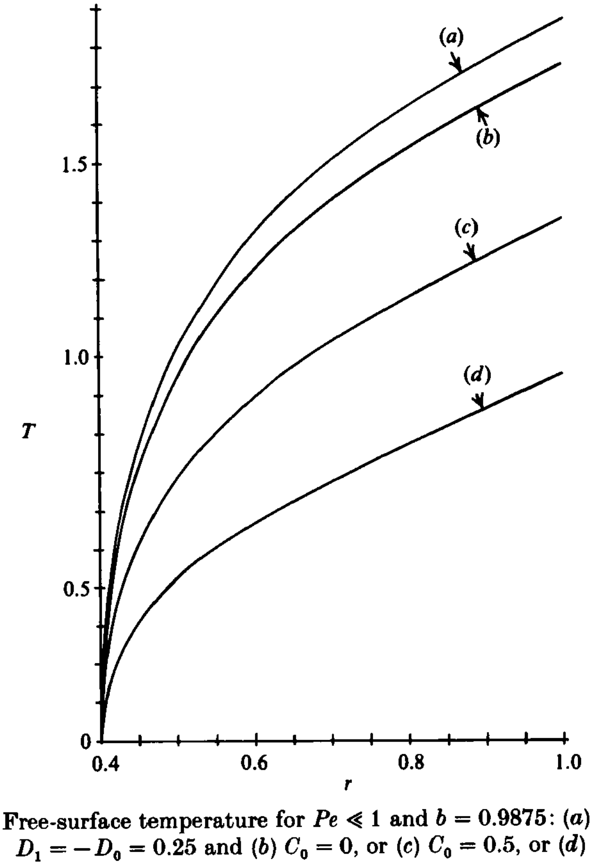

FIGURE 4. Free-surface temperature for $Pe \ll 1$ and $b = 0.9875$: (a) $C_0 = D_0 = D_1 = 0$; $D_1 = -D_0 = 0.25$ and (b) $C_0 = 0$, or (c) $C_0 = 0.5$, or (d) $C_0 = 1$.

dimensionless solution (10) for the melt motion due to buoyancy is insensitive to changes in C_0, D_0 and D_1, but the value of U, which is used to translate these dimensionless results into dimensionless velocities, does depend on these thermal coefficients. For case (*a*) in figure 4, very little heat is lost through the free surface or crucible bottom, so that a relatively small q is needed to maintain a given free-surface temperature difference, and the buoyancy-driven melt velocities are relatively small. For case (*d*) in figure 4, much more heat is lost through the free surface and bottom, so that q must be larger to maintain the free-surface temperature difference, and the buoyancy-driven melt velocities are nearly twice those for case (*a*). The values of C_0, D_0 and D_1 are certainly not controllable parameters; we consider the effects of changing these coefficients because of the uncertainty about their values in an actual crystal puller.

The expression (18) indicates that the magnitude of the buoyancy-driven circulation decreases like b^2 as the depth decreases.

4. Melt motion due to thermocapillarity

In this section we drop the buoyancy term T in (2*b*) in order to consider the flow due to thermocapillarity alone. In the outer core (o) for $a < r < 1$, the variables v_{ro}, v_{zo}, $j_{\theta o}$, p_o and T_o are all $O(1)$, while

$$v_{ro} = -j_{\theta o} = \frac{1}{r}\frac{\partial \psi_o}{\partial z}, \quad v_{zo} = -\frac{1}{r}\frac{\partial \psi_o}{\partial r} \tag{19a, b}$$

satisfy (2*c*, *d*) for any outer-core stream function $\psi_o(r, z)$.

The melt motion in the free-surface Hartmann layer (h) at $z = b$ for $a < r < 1$ is driven by the boundary condition (5*b*), and this motion in turn drives the motion in other subregions of the melt. For this Hartmann layer we stretch the axial coordinate by introducing $z = b + M^{-1}Z$. The $O(1)$ temperature and pressure are continuous across this layer, so that

$$T = T_o(r, b) + M^{-1}T_h(r, Z),$$

with a corresponding expression for p. In addition v_r and j_θ are $O(M)$, while v_z is $O(1)$. For $Pe = O(1)$, (2*a*–*e*) without the inertial or buoyancy terms give

$$v_{rh} = -j_{\theta h} = \frac{1}{r}\frac{\partial \psi_h}{\partial Z}, \quad v_{zh} = -\frac{1}{r}\frac{\partial \psi_h}{\partial r}, \tag{20a, b}$$

$$\frac{\partial^3 \psi_h}{\partial Z^3} = \frac{\partial \psi_h}{\partial Z}, \quad \frac{\partial p_h}{\partial Z} = -\frac{1}{r}\frac{\partial^3 \psi_h}{\partial r\, \partial Z^2}, \tag{20c, d}$$

$$\frac{\partial^2 T_h}{\partial Z^2} = \frac{Pe}{r}\frac{\partial T_o}{\partial r}(r, b)\frac{\partial \psi_h}{\partial Z}, \tag{20e}$$

where $\psi_h(r, Z)$ is the free-surface Hartmann-layer stream function. The boundary conditions (5), (6) become

$$\psi_h = 0, \quad \frac{\partial^2 \psi_h}{\partial Z^2} = -Qr\frac{\partial T_o}{\partial r}(r, b), \tag{21a, b}$$

$$\frac{\partial T_h}{\partial Z} = -C_0 - C_1 T_o(r, b) \quad \text{at } Z = 0. \tag{21c}$$

Matching the outer core gives

$$\psi_{\mathrm{h}} \rightarrow \psi_0(r,b), \quad \frac{\partial T_{\mathrm{h}}}{\partial Z} \rightarrow \frac{\partial T_0}{\partial z}(r,b) \quad \text{as } Z \rightarrow -\infty. \tag{22a,b}$$

Equation (20*e*) is integrated with respect to Z and the boundary conditions (21*a*, *c*) are used to determine the integration function of r. The result is

$$\frac{\partial T_{\mathrm{h}}}{\partial Z} = \frac{Pe}{r}\frac{\partial T_0}{\partial r}(r,b)\,\psi_{\mathrm{h}} - C_0 - C_1\,T_0(r,b). \tag{23}$$

The matching conditions (22) now give

$$\frac{\partial T_0}{\partial z}(r,b) = \frac{Pe}{r}\psi_0(r,b)\frac{\partial T_0}{\partial r}(r,b) - C_0 - C_1\,T_0(r,b) \tag{24}$$

for the jump in the axial heat flux across the free-surface Hartmann layer. Since both ψ_0 and $\partial T_0/\partial r$ are positive, this Hartmann layer represents a radially inward jet which is adjacent to the free surface and which is driven by the radial gradient of the surface tension. This jet draws hot fluid from below near the vertical crucible wall and returns cold fluid near the crystal edge. The heat rejected by this jet provides some of the heat lost through the free surface, so that the outer core sees a smaller heat loss at $z = b$. The solution of (20*c*) that satisfies the conditions (21 *a*, *b*) and that does not grow exponentially as $Z \rightarrow -\infty$ is

$$\psi_{\mathrm{h}} = Qr\frac{\partial T_0}{\partial r}(r,b)[1-\exp(Z)]. \tag{25}$$

The Hartmann-layer velocities, electric-current density and $O(M^{-1})$ pressure variation are now given by (20*a*, *b*, *d*). The core matching (22*a*) gives the boundary condition

$$\psi_0(r,b) = Qr\frac{\partial T_0}{\partial r}(r,b) \tag{26}$$

on the outer-core stream function. This condition merely states that the $O(1)$ inward flow in the free-surface Hartmann layer must be balanced by an equal outward flow in the outer core. The outer-core solution that satisfies (2*a*, *b*), (19), without the inertial, viscous and buoyancy terms, and that satisfies the boundary condition (26) is

$$\psi_0 = \frac{Q}{b}rz\frac{\partial T_0}{\partial r}(r,b), \quad p_0 = -\frac{Q}{b}T_0(r,b). \tag{27a,b}$$

The deflection $f(r)$ of the free surface due to thermocapillarity is given by $\alpha(\Delta T)$ times (27*b*). There are no high-velocity jets in the Hartmann layers on the crystal face or crucible bottom because there are no $O(M^2)$ shear stresses on these layers. The radial outer-core velocity (19*a*), (27*a*) is independent of z and is proportional to the local free-surface temperature gradient.

An $O(1)$ flow enters the vertical wall layer (w) from the outer core at $r = 1$. This fluid flows upward inside this layer and enters the intersection region (I) at $r = 1$ and $z = b$. It then flows inward inside this region and enters the free-surface Hartmann layer at $r = 1$. The analysis for the vertical wall layer and adjacent intersection region at $z = b$ parallels that discussed in §3. The treatment of the intersection region is somewhat more complex because this region is now part of the $O(1)$ flow circuit. Since there is no buoyancy, (17) reduces to

$$\frac{\partial^2 \psi_{\mathrm{w}}}{\partial z^2} = \frac{\partial^4 \psi_{\mathrm{w}}}{\partial R^4}. \tag{28}$$

This equation with appropriate boundary conditions is solved by the separation-of-variables method, and the result is a series solution which converges with a few terms. Equation (15) holds for all R, and matching the outer core gives

$$\frac{\partial T_o}{\partial r}(1,z) = 1 - Pe\,\psi_o(1,z)\frac{\partial T_o}{\partial z}(1,z) \tag{29}$$

for the jump in the $O(1)$ radial heat flux across the vertical wall layer due to thermocapillarity. For the present analysis, the only other important aspect of the vertical wall layer and adjacent intersection region at $z = b$ is that the former accepts any uniform radial velocity from the outer core and the latter returns an equal flow to the free-surface Hartmann layer. Vertical-wall-layer velocity profiles for the melt motion due to thermocapillarity will be presented in a future paper treating the mass transport associated with these melt motions.

Thermocapillarity does not produce any motion in the inner core or adjacent Hartmann layers, i.e. $\psi_i = 0$. The intersection region at $r = a$ and $z = b$ accepts an $O(1)$ flow from the free-surface Hartmann layer at $r = a$ and delivers an equal flow to the free-shear layer at $z = b$. This fluid flows down the free-shear layer and enters the outer core as a uniform radial velocity at $r = a$. To study the structures of the free-shear layer and adjacent intersection region at $z = b$, we stretch the radial coordinate by introducing $r = a + M^{-\frac{1}{2}}R$. The free-shear-layer solution matches the inner and outer cores as $R \to -\infty$ and $+\infty$, respectively. Equation (28) with w replaced by f holds and is solved by separation of variables. The $O(1)$ temperature and pressure are continuous across the free-shear layer so that

$$T_i(a,z) = T_o(a,z). \tag{30}$$

The integration of (11c) governing the $O(M^{-\frac{1}{2}})$ perturbation temperature $T_f(R,z)$ and the matching with the outer-core variables as $R \to \infty$ give

$$\frac{\partial T_f}{\partial R}(R,z) = \frac{\partial T_o}{\partial r}(a,z) + Pe\frac{\partial T_o}{\partial z}(a,z)\left[\psi_o(a,z) - \psi_f(R,z)\right].$$

The matching with the inner-core variables as $R \to -\infty$ now gives

$$\frac{\partial T_i}{\partial r}(a,z) = \frac{\partial T_o}{\partial r}(a,z) + Pe\frac{\partial T_o}{\partial z}(a,z)\left[\psi_o(a,z) - \psi_i(a,z)\right] \tag{31}$$

for the jump in the radial heat flux across the free-shear layer due to thermocapillarity. For the fluid entering the free-shear layer at $z = b$, the temperature $T = 0$. As this fluid descends, its temperature rises ($\partial T/\partial z < 0$), and the fluid absorbs some of the heat flowing into the free-shear layer from the outer core. For the melt motion due to thermocapillarity alone, $\psi_i = 0$, but we leave ψ_i in the jump condition (31) because in §6 we apply the jump conditions (24), (29)–(31) using a ψ_o equal to the sum of (10c), (27a) with $T_c = T_o$ and using ψ_i equal to (10c) with $T_c = T_i$. Considered by itself the melt motion due to buoyancy does not involve a free-shear layer at $r = a$. However, the melt motion due to thermocapillarity produces a jump (31) in $\partial T/\partial r$ across the free-shear layer, so that (10c) indicates that there is now a jump in the stream function for the buoyancy-driven flow. The free-shear layer accommodates the downward flows associated with thermocapillarity and with this modification of the buoyancy-driven flow.

The melt motion driven by thermocapillarity and the effects of changing the thermal coefficients C_0, D_0 and D_1 are illustrated in this section with the $T(r,z)$ for

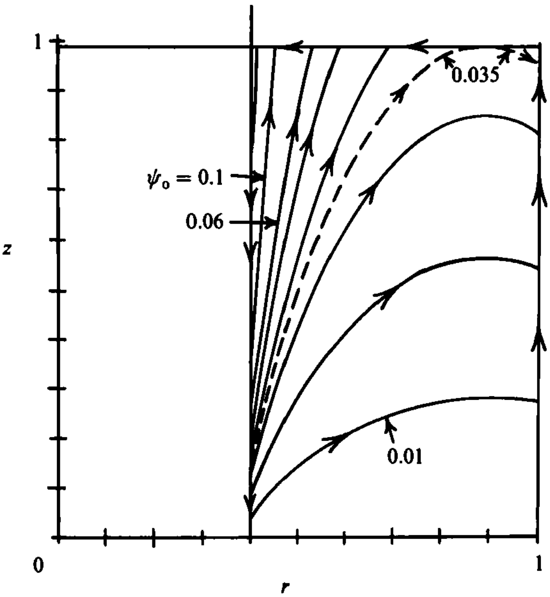

FIGURE 5. Streamlines for thermocapillarity only and with $Pe \ll 1$, $b = 0.9875$, $C_0 = 0$, and $D_1 = -D_0 = 0.25$. Here $\psi_0 = 0.01, 0.02, 0.03, 0.035, 0.04, 0.05, 0.06, 0.1$ and 0.2. The upward flow inside the vertical wall layer, the inward flow inside the free-surface Hartmann layer and the downward flow inside the free-shear layer are represented by the lines at $r = 1$, $z = b$ and $r = a$, respectively.

$Pe \ll 1$ and $b = 0.9875$. The general conclusions about the effects of changing the thermal coefficients are equally true for any b and $Pe < 10$. The streamlines for $C_0 = 0$ and $D_1 = -D_0 = 0.25$ are shown in figure 5. This motion is driven by the inward flow inside the free-surface Hartmann layer, and this flow is proportional to the local radial heat flux $r\,\partial T/\partial r$ at the free surface. For a constant radial heat flux, $r\,\partial T/\partial r$ would be one for all r, and the outer-core streamlines in figure 5 would be a set of horizontal lines for the return flow from the free-shear layer to the vertical wall layer. This is not the case because the radial heat flux at the free surface is not a constant. The boundary condition (7c) gives $\psi_0(1,b) = Q = 0.036$ for $Pe \ll 1$. As we move inward along the free surface from the crucible, the local radial heat flux first decreases slightly because of heat lost through the free surface here. For $C_0 = 0$, the value of $\psi_0(r,b)$ decreases slightly to 0.035 at $r = 0.9$, so that a small fraction of the inward flow leaves the Hartmann layer and returns to the vertical wall layer through the outer core. This gives a very weak counterclockwise circulation near $r = 1$ and $z = b$. Since much of the heat eventually enters the crystal at $z = b$, there is an axial heat flux toward the top. For $C_0 = 0$, the axial heat flux toward the free surface from below exceeds the heat lost through the free surface for $r < 0.9$, so that $r\,\partial T/\partial r$ and ψ_0 at $z = b$ increase as r decreases from 0.9. The free-surface Hartmann layer draws fluid from the outer core until $\psi_0(a,b) = 0.24$ for this case, so that there is nearly seven times as much flow inside the Hartmann layer at $r = a$ as at $r = 1$. The flow turns down into the free-shear layer and completes its circuit through the outer core. There is a very strong, axially elongated, counterclockwise circulation near the crystal edge. This circulation is driven by the large value of $r\,\partial T/\partial r$ near $r = a$ and $z = b$ which is associated with the convergence of the heat flux toward the crystal face.

The streamlines for $C_0 = D_0 = D_1 = 0$ or for $D_1 = -D_0 = 0.25$ and $C_0 = 0.5$ or 1.0

are similar to those in figure 5. The principal effect of changing these coefficients is to change the magnitude of the strong circulation near $r = a$. For each case $\psi_0(1, b) = 0.036$, but $\psi_0(a, b) = 0.26, 0.24, 0.17$ and 0.10 for cases (*a*), (*b*), (*c*) and (*d*) in figure 4, respectively. Changing D_0 and D_1 has a minor effect on the free-surface temperature (cases *a* and *b* in figure 4) and hence has very little effect on the melt motion due to thermocapillarity. Changing C_0 (cases *b*, *c* and *d* in figure 4) has a relatively minor effect on $\partial T/\partial r$ at $z = b$ for $0.65 < r < 1$, but has a strong effect for $0.4 < r < 0.5$. The boundary condition (6) gives the axial heat flux through the free surface. When we change C_0 from 0 to 1, this heat flux at $r = 1$ only changes from 0.87 to 1.48, but this heat flux at $r = a$ changes from 0 to 1.0. With $C_0 = 0$, there is no heat loss through the free surface at $r = a$ and the local radial temperature gradient becomes very large. With $C_0 = 1$, there is still a significant heat loss through the free surface near $r = a$, $\partial T_0/\partial r$ at $r = a$, $z = b$ is much smaller than it is for $C_0 = 0$, and the circulation near $r = a$ is much weaker. Therefore the only important effect of changing C_0 is the resultant change in the heat flux through the free surface near the crystal edge, which in turn controls the magnitude of the melt circulation near $r = a$.

An estimate of the heat loss through the free surface near the crystal edge is needed in order to determine the magnitude of the melt circulation near $r = a$ due to thermocapillarity. All parts of the free surface, exposed crystal surface, unwetted crucible wall and furnace wall are emitting, absorbing and reflecting radiation. Aspects of these radiation problems have been treated by Ramachandran & Dudukovic (1985) and by Srivastava, Ramachandran & Dudukovic (1985, 1986). In their treatment the exposed crystal surface and the free surface are divided into many sections, each with a different temperature. The unwetted crucible wall and furnace wall have two different, uniform temperatures. Each isothermal surface emits radiation, absorbs radiation emitted by each of the other surfaces and absorbs radiation reflected by each of the other surfaces. The final result is a set of simultaneous equations which are solved numerically. Stern (1985) develops a similar treatment. We use a two-step, approximate treatment to estimate the heat loss through the free surface near the crystal edge.

In the first step, we treat black-body radiation ($\epsilon = 1$ and no reflection for all surfaces). The exposed crystal surface is at $r = a$ for $b < z < b + L_s$; the unwetted crucible wall is at $r = 1$ for $b < z < b + L_c$; the furnace wall is at $r = 1$ for $b + L_c < z < b + L_w$ and at $z = b + L_w$ for $0 < r < 1$. We compute the radiation view factors for a differential area of the free surface at r and take the limit as $r \rightarrow a$. The temperature variation along the crystal and L_s do not matter because the free-surface element adjacent to the crystal edge only receives radiation from the part of the crystal surface near $z = b$ which is at $T^* = T_s = 1685$ K. The temperature variation along the free surface does not matter because an element of the free surface does not receive radiation from the rest of the free surface since there is no reflection. The furnace wall and unwetted crucible wall are assumed to have different, uniform temperatures, T_{fw} and T_{uc}, respectively. The result is a formula for the radiation received by the free-surface differential area at $r = a$ from the crystal surface, unwetted crucible wall and furnace wall.

The approximation is introduced in the second step to estimate the effects of partial emissivity ($\epsilon < 1$) and reflection. The results of the first step are converted into an equivalent one-dimensional radiation problem with two parallel planes. The first plane represents the differential area adjacent to the crystal edge and has $T^* = T_s$, while the second plane represents the crystal surface, unwetted crucible wall and furnace wall. The second plane has $T^* = T_{\mathrm{ebb}}$, the effective background temperature to give the same black body radiation to the free-surface element. We then let $\epsilon = 0.318$ and 0.59 for the first and second planes respectively, and we let the reflectivity of each plane equal $1-\epsilon$ (Ramachandran & Dudukovic 1985). The balance of incident, reflected, emitted and absorbed radiation at each plane leads to an estimate of the increase in the radiation absorbed by the free-surface element because of partial emissivity and reflection. We take $T_{\mathrm{fw}} = 373$ K, $T_{\mathrm{uc}} = 1785$ K, $L_{\mathrm{w}} L = 1.0$ m (tall enough to hold a 1.0 m long crystal) and $L_{\mathrm{c}} L = 3.0$, 7.7 and 10.1 cm for $b = 1.0$, 0.5 and 0.25, respectively. As the crystal is pulled, the increase in L_{c}, the height of the unwetted crucible wall, equals the decrease in b. The results give an equivalent background temperature T_{e} for the free-surface differential area adjacent to the crystal edge: $T_{\mathrm{e}} = 1490$ K and $C_0 = 0.66$ for $b = 1.0$; $T_{\mathrm{e}} = 1624$ K and $C_0 = 0.232$ for $b = 0.5$; $T_{\mathrm{e}} = 1659$ K and $C_0 = 0.101$ for $b = 0.25$. A free-surface element at a larger r would have a higher T_{e} and smaller C_0 because it is closer to the hot unwetted crucible wall. However, we have seen that only the heat loss through the free surface near $r = a$ is critical for the melt motion. If we use these values of C_0 for the entire free surface, we will overestimate the heat loss through the free surface near the crucible, but the melt motion is relatively insensitive to the heat flux near $r = 1$. For $C_0 = 0.66$, $C_1 = 0.496$, $D_1 = -D_0 = 0.25$, $Pe \ll 1$, $a = 0.4$ and $b = 0.9875$, $\psi_0(a, b) = 0.15$, which indicates the actual magnitude of the melt circulation due to thermocapillarity near $r = a$. In §§5 and 6 we use these estimated values of C_0 for a number of cases with various values of b and Pe.

The result (26) indicates that the magnitude of the melt circulation due to thermocapillarity is independent of the depth bL, except through the dependence of the free-surface temperature on depth. Since the magnitude of the buoyancy-driven circulation decreases like b^2, we expect thermocapillarity to become progressively more dominant as the depth decreases.

In this paper we use the traditional bulk-flow approximation in which the crystal face and free surface are assumed to lie in the same horizontal plane (Langlois 1981). In reality there is a meniscus: at the crystal edge the free surface is at an angle of 11° to the vertical, rather than 90°, and as r increases from a, the free surface curves down towards a horizontal plane which is below the crystal edge. Does the strong, axially elongated thermocapillary convection near $r = a$ occur when the meniscus is included? The first effect of the meniscus is to reduce the temperature gradient along the free surface near the crystal edge. The large values of $\partial T/\partial r$, at $r = a$, $z = b$, in figure 4 are associated with the heat conduction around a sharp, 90° corner. With the meniscus, the heat flows around a corner with a finite radius of curvature, and the temperature gradient at the corner is much less. Srivastava *et al.* (1985) solve for the heat conduction in the melt and crystal with radiation from both surfaces. They treat both a horizontal free surface with a sharp, 90° corner at the crystal edge and a free surface with a meniscus rising to an 11° angle at the crystal edge. From the isotherms for the two cases, it appears that the temperature gradient along the free surface at the crystal edge is reduced by a factor of two or three by the addition of the meniscus. This effect has been incorporated into the present calculations. When we evaluate $\partial T_0/\partial r$, at $r = a$, $z = b$, for the thermocapillary stream function (27*a*), we do not use the slopes of the curves in figure 4 at $r = a$. Instead we use

$$h^{-1}[T(a+0.5h, b) - T(a-0.5h, b)],$$

where $h = 0.025$ is the grid spacing for our finite-difference treatment of (2*e*). This gives free-surface temperature gradients at $r = a$ which are one-third to one-half those in figure 4. In essence, we are assuming that the radius of curvature of the meniscus is comparable with h.

The second effect of the meniscus is to change the optical orientation of the free-surface element adjacent to the crystal edge. Because of this change, this element receives more radiation from the hotter free surface and unwetted crucible wall and less radiation from the colder crystal and furnace wall. This change increases T_e, reduces the net radiant heat loss for this element, and increases the free-surface temperature gradient here. This effect is included in the numerical results presented by Srivastava *et al.* (1985).

The third effect of the meniscus is to change the structure of the free-surface Hartmann layer because the local free surface is no longer perpendicular to the magnetic field. To treat this Hartmann layer, we use an orthogonal curvilinear coordinate system (t, θ, n), where t is the distance along the free surface from the crystal edge and n is the distance along the local normal to the free surface, out of the melt. We stretch the normal coordinate by substituting $n = M^{-1}N$. To first order, the surface curvature has no effect, and the principal change is that $\exp(Z)$ is replaced by

$$\exp(N \cos\lambda),$$

where $\lambda = \arccos(\hat{z}\cdot\hat{n})$ is the local angle between $\hat{z}$, the unit vector parallel to the magnetic field, and $\hat{n}$, the unit normal to the free surface. The thickness of a Hartmann layer is inversely proportional to the normal component of the magnetic field, so that the thickness of the free-surface layer increases as λ increases from zero. The tangential shear stress in a layer is proportional to the tangential velocity divided by the layer thickness. Since the boundary condition (5*b*) prescribes a specific shear stress at the free surface, the tangential velocity must increase as $\sec\lambda$ to compensate for the increase in the layer thickness, as λ increases. The total flow inside the layer at a given point on the free surface is given by the integral of the increased tangential velocity over the increased boundary-layer thickness. Therefore the boundary condition (26) on the outer-core stream function is replaced by

$$\psi_0 = Qr\sec^2\lambda\frac{\partial T_0}{\partial t} \quad \text{at } n = 0,$$

where r and λ are functions of t (D. N. Riahi & J. S. Walker 1987, paper in preparation). As we move inward along the meniscus towards the crystal edge, the flow driven by thermocapillarity for a given temperature gradient is amplified by a factor equal to $\sec^2\lambda$. This factor reaches a value of 27.5 for $\lambda = 79°$ at the crystal edge.

The radius of curvature of the meniscus, normalized by the crucible radius, is rather small. Therefore we might assume that it is comparable with $M^{-\frac{1}{2}}$, so that the meniscus occupies the part of the free surface above the free-shear layer at $r = a$. For this case, the analysis for the intersection region (I), which now follows the free surface with $\Delta n = O(M^{-1})$ and $\Delta t = O(M^{-\frac{1}{2}})$, is exactly the same as that for the meniscus above the outer core. The increase in the tangential gradient is insufficient to change the Hartmann-layer solution, which retains its local structure, $\exp(N\cos\lambda)$. Therefore, the same $\sec^2\lambda$ amplification of the thermocapillary motion occurs inside the free-shear layer. As we approach the crystal edge, the acceleration of the free-surface jet continues until we enter the $O(M^{-1}) \times O(M^{-1})$ viscous region at the crystal edge. For $B = 0.1$–1.0 T, this is a very small region. Inside this region, the free surface jet turns to enter the free-shear layer as a flow source at $r = a$, $z = b$.

For magnetic Czochralski flows, the bulk-flow approximation implicitly assumes that the dimensionless radius of curvature of the meniscus is comparable with M^{-1}.

The effects of the meniscus are to reduce the free-surface temperature gradient at the crystal edge and to increase the thermocapillary flow near $r = a$ due to changes in the free-surface Hartmann-layer structure. The latter implies extremely strong flow accelerations near the crystal edge, and these accelerations are probably limited by inertial effects, which are ignored here. The results presented here ignore the meniscus and involve strong thermocapillary convection near $r = a$. Combining the two effects of the meniscus, we conclude that the present analysis underestimates the thermocapillary convection that would occur in an actual puller with a meniscus.

5. Combined motions for $Pe \ll 1$ and several depths

Figure 6 presents the streamlines for the melt motion due to both buoyancy and thermocapillarity with the $T(r, z)$ for $Pe \ll 1$. Figure 6(*a*) represents the combination of the streamlines in figures 3 and 5 for $b = 0.9875$, except that $C_0 = 0.66$ instead of 0. For this depth the circulations due to buoyancy and thermocapillarity are almost equal. The maximum values of the separate stream functions are 0.12 and 0.15 for buoyancy and thermocapillarity, respectively. There are three types of streamlines in figure 6(*a*). The streamlines for $0 < \psi < 0.036$ (i) go upward inside the vertical wall layer at $r = 1$ from near the bottom ($z < 0.07$) to the free surface, (ii) go inward inside the free-surface Hartmann layer at $z = b$ from the crucible to the crystal edge, (iii) go downward a short distance inside the free-shear layer at $r = a$, (iv) go downward inside the inner core near $r = a$ and return to the free-shear layer, (v) go downward a short distance inside the free-shear layer, and (vi) go across the outer core near the bottom ($z < 0.17$) to the vertical wall layer. These streamlines account for all of the flow entering the inner core beneath the crystal face. The streamlines for $0.036 < \psi < 0.085$ (i) go upward inside the vertical wall layer from near the bottom ($0.07 < z < 0.2$) to near the free surface ($0.86 < z < b$), (ii) go inward across the outer core until they enter the free-surface Hartmann layer near the crystal edge, (iii) go a short distance inside the free-surface Hartmann layer to the crystal edge, (iv) go downward inside the free-shear layer to $0.13 < z < 0.35$, and (v) go outward across the outer core to the vertical wall layer. The streamlines for $0.085 < \psi < 0.15$ represent two separate melt circulations. The first involves a counterclockwise circulation through the vertical wall layer and the outer core in the region $0.6 < r < 1$ and $0.2 < z < 0.86$. The second involves a counterclockwise circulation through the free-surface Hartmann layer, free-shear layer and outer core in the region $0.4 < r < 0.5$ and $0.35 < z < b$.

The streamlines for an intermediate stage in the growth of a crystal when $b = 0.4875$ are shown in figure 6(*b*). For this depth, the circulation due to thermocapillarity is nearly four times that due to buoyancy. The maximum values of the

---

FIGURE 6. Streamlines for the melt motion due to both buoyancy and thermocapillarity with $Pe \ll 1$. Upward flow inside the vertical wall layer, inward flow inside the free-surface Hartmann layer and downward flow inside the free-shear layer are represented by the lines at $r = 1$, $z = b$ and $r = a$, respectively. (*a*) $b = 0.9875$, $C_0 = 0.66$, $D_1 = -D_0 = 0.25$, and $\psi = 0.01m$, for $m = 1$–14. Some streamlines near $r = a$ and $z = b$ are not shown. (*b*) $b = 0.4875$, $C_0 = 0.232$, $D_0 = 0$, $D_1 = 0.25$, $\psi_i = 0.002m$, for $m = 1$–6 in the inner core, and $\psi_o = 0.004m$, for $m = 1$–12, plus $\psi_o = 0.06$, 0.1 in the outer core. (*c*) $b = 0.2375$, $C_0 = 0.101$, $D_0 = 0$, $D_1 = 0.5$, $\psi_i = 0.001$, 0.002, 0.003 in the inner core, and $\psi_o = 0.004m$, for $m = 1$–10, plus $\psi_o = 0.05$, 0.06, 0.07 in the outer core.

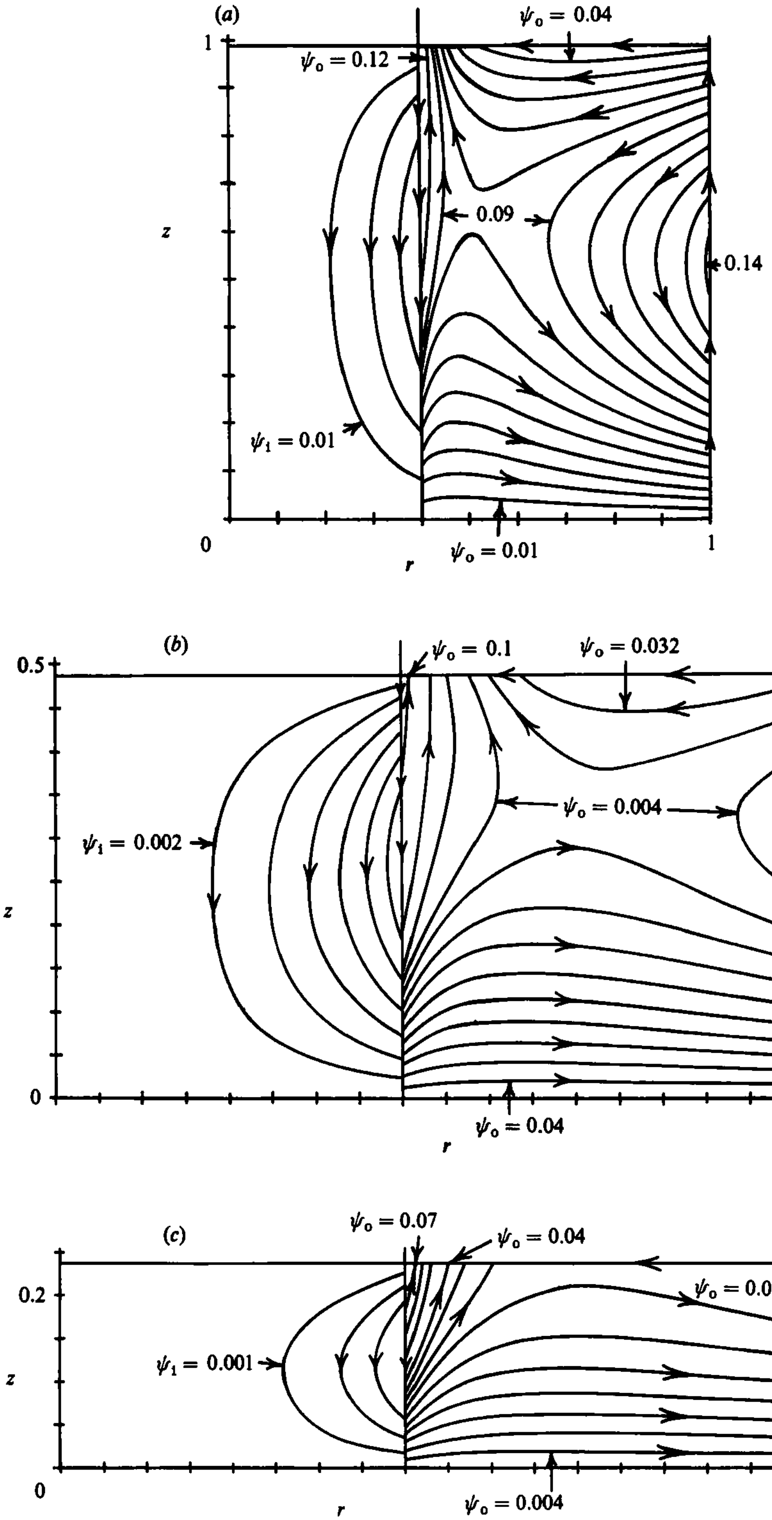

FIGURE 6(*a*–*c*). For caption see facing page.

separate stream functions are 0.03 and 0.11 for buoyancy and thermocapillarity, respectively. The three types of streamlines described for $b = 0.9875$ still occur, but the values of ψ for each type are different. For the first type of streamline, which penetrate into the inner core, $0 < \psi < 0.012$, so that the flow into the inner core is one-third that for $b = 0.9875$. For the second type of streamline, which go from $r = 1$ to a near the free surface and return from $r = a$ to 1 near the bottom, $0.012 < \psi < 0.038$, so that this circulation is roughly half that for $b = 0.9875$. For these streamlines the inward flow is now divided between the free-surface Hartmann layer and the outer core. The third type of streamline again represents two separate, local, counterclockwise circulations. As b decreases from 0.9875 to 0.4875, the local circulation through the free-surface Hartmann layer, free-shear layer and outer core near $r = a$ and $z = b$ remains essentially unchanged. For both values of b, this circulation corresponds to $\Delta\psi = 0.07$. However the local circulation through the vertical wall layer and the outer core near $r = 1$ and $z = 0.6b$ diminishes from $\Delta\psi = 0.06$ for $b = 0.9875$ to $\Delta\psi = 0.012$ for $b = 0.4875$.

The streamlines for a final stage in the growth of a crystal when $b = 0.2375$ are shown in figure 6(*c*). For this depth the circulation due to thermocapillarity is twelve times that due to buoyancy. The maximum values of the separate stream functions are 0.007 and 0.086 for buoyancy and thermocapillarity, respectively. For the first type of streamline, which penetrate into the inner core, $0 < \psi < 0.004$, so that the flow in the inner core is one-ninth that for $b = 0.9875$. The streamlines in the outer core are very similar to the streamlines for thermocapillarity alone. For the second type of streamline, with circulation from $r = 1$ to a and back, $0.004 < \psi < 0.03$ and the inward flow is entirely inside the free-surface Hartmann layer. There is only outward flow in the outer core. For the third type of streamline, with separate circulations near $r = a$ and $r = 1$, the circulation near $r = a$ and $z = b$ has diminished slightly to $\Delta\psi = 0.055$ from $\Delta\psi = 0.07$ for $b \geqslant 0.4875$. The circulation near $r = 1$ and $z = 0.6b$ has disappeared and has been replaced by the weak circulation near $r = 1$ and $z = b$, which is associated with thermocapillarity as described in §4.

6. Combined motion for various values of *Pe*

In the present analysis the Péclet number *Pe* reflects the magnetic field strength *B*. As *B* is increased, *U* and hence *Pe* decrease like B^{-2}. The solutions in §§3 and 4 for the stream functions in terms of the unknown temperature $T(r, z)$ are valid for any *Pe*. We have illustrated the characteristics of these melt motions with the $T(r, z)$ for $Pe \ll 1$ corresponding to a strong magnetic field. Here we consider the melt motions for the $T(r, z)$ for other values of *Pe*.

Equation (2*e*) is solved separately for the temperatures T_i and T_0 in the inner and outer cores. For the outer core, the velocities for the left-hand side of (2*e*) are given by the sum of the stream functions (10*c*), (27*a*) with $T_c = T_0$. For the inner core, only the stream function (10*c*) with $T_c = T_i$ is used. The outer-core temperature satisfies the boundary conditions (8*c*), (24), (29), again with ψ_0 given by the sum of the stream functions (10*c*), (27*a*). The inner-core temperature satisfies the boundary conditions (4*c*), (8*c*), (9*b*). The inner- and outer-core temperatures are coupled by the jump conditions (30), (31). These coupled boundary-value problems are solved numerically using a finite-difference method.

The isotherms for $b = 0.9875$ and for $Pe \ll 1$ (large *B*) or $Pe = 3$ ($B = 0.188$ T) or $Pe = 10$ ($B = 0.103$ T) are presented in figures 7(*a*–*c*). Figure 7(*d*) presents (*a*) the temperature of the free surface at the first grid point beyond the crystal edge, (*b*) the temperature of the free surface at the crucible wall, (*c*) the temperature at the bottom of the vertical wall, and (*d*) the temperature at the centre of the crucible bottom.

As the Péclet number increases (B decreases), the temperature everywhere on the bottom decreases and the temperature of the free surface near the crystal increases. Cold fluid is carried from near the crystal and free surface to the bottom, while hot fluid is carried from the vertical crucible wall to the free surface and inward toward the crystal. As Pe increases from 0 to 6, the temperature of the free surface at the crucible increases as hot fluid is carried up to the free surface. As Pe increases, thermal convection carries an increasing fraction of the total heat flux from the vertical crucible wall to the free surface and crystal. Therefore the fraction carried by thermal conduction and the associated temperature difference between the crucible and crystal decrease. As Pe first increases from zero, the fraction of the heat flux carried by convection is still very small, so that the average temperature of the vertical crucible wall remains almost constant. The principal effect of convection for small values of Pe is to make the isotherms more vertical, so that the top and bottom become hotter and colder, respectively. However, for $Pe > 6$, the reduction in the fraction of the total heat flux carried by thermal conduction becomes significant, the mean temperature of the vertical crucible wall drops significantly, and the free surface at the crucible cools as Pe increases above 6.

The isotherms $T = 0.6$ for $Pe = 3$ and $T = 0.8$ for $Pe = 10$, actually bend inwards slightly at the free surface, indicating a heat flux into the outer core from the free surface. The jet driven by thermocapillarity inside the free-surface Hartmann layer is cooling as it moves radially inward. The heat it loses reduces the heat flux from the outer core at the free surface for all r. Near $r = a$, the heat rejected by this surface jet exceeds the local radiation from the free surface, so that the outer core sees a small heat input at $z = b$.

Because of our definition of the dimensionless temperature, the preceding discussion assumes that the heat input to the vertical crucible wall is the same for all magnetic-field strengths. If the heat input is adjusted to give the same temperature difference at the free surface between the crystal and crucible, then curve (*b*) in figure 7 (*d*) indicates that the required heat input decreases slightly as B is increased from 0.103 to 0.133 T ($Pe = 6$) and then increases as B increases from 0.133 T to ∞. For large B, the required heat flux is 25 % more than that for $B = 0.103$ T. In reality, flaring is a function of the radial temperature gradient near the crystal edge, rather than of the overall temperature difference at the free surface, and this temperature gradient is proportional to curve (*a*) in figure 7 (*d*). To maintain a constant value of $\partial T/\partial r$ at $r = a$ and $z = b$, the heat input must increase as B is increased and the heat flux for large B is 2.75 times that for $B = 0.103$ T. Therefore, for constant radial temperature gradient at the crystal edge, the elevation of the crucible temperature at the free surface above $T_s = 1685$ K for large B is 2.2 times that for $B = 0.103$ T. Since the rate at which the silicon melt dissolves the quartz crucible increases with increasing local temperature, much more oxygen may enter the melt for strong magnetic fields than for weak ones, if $\partial T/\partial r$ at $r = a$ and $z = b$ is kept constant to prevent flaring.

The heat flux to the crystal is more uniform for a strong magnetic field than for a weak one. For $Pe \ll 1$, figure 7 (*a*) indicates that the heat flux is nearly uniform over most of the crystal face with a modest increase near the crystal edge. For $Pe = 3$, figure 7 (*b*) indicates that heat fluxes near $r = 0$ and $r = a$ are respectively somewhat less and more than those for $Pe \ll 1$, but the differences are less than 10 %. However,

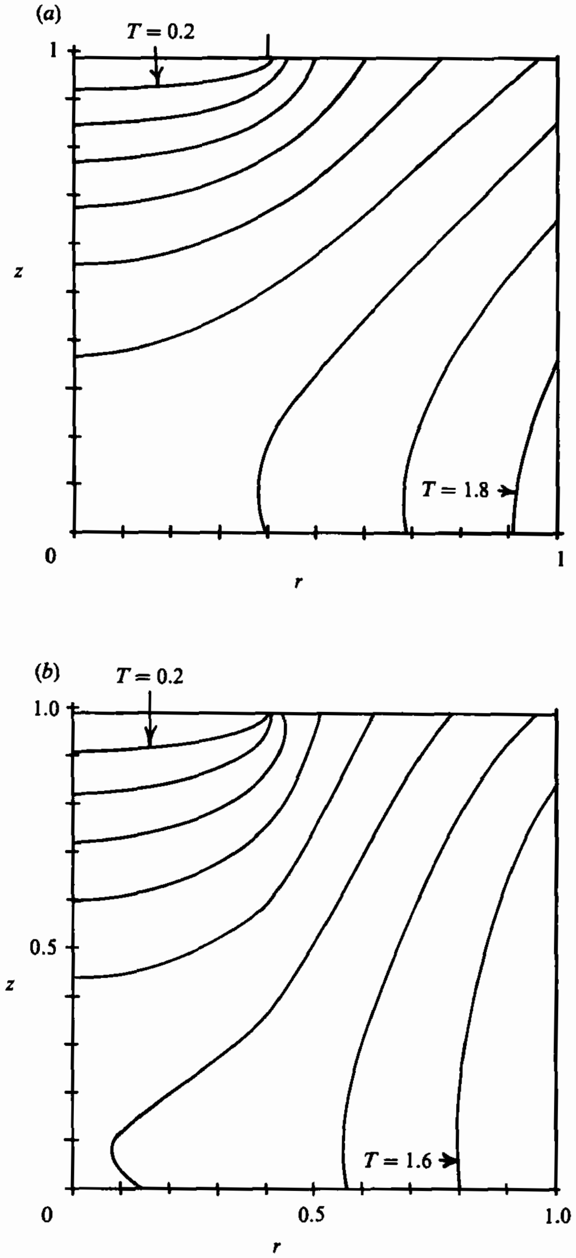

FIGURE 7 (*a*, *b*). For caption see facing page.

for $Pe = 10$, the heat fluxes near $r = 0$ and $r = a$ are respectively roughly half and twice those for $Pe \leqslant 1$. All of the fluid that travels from $r = 1$ to $r = a$ either travels entirely inside the free-surface Hartmann layer or enters this Hartmann layer near $r = a$. Therefore, once thermal convection becomes significant, the flow delivers a large amount of heat to the region very near the crystal edge, so the heat enters the crystal here. The corresponding reduction in thermal conduction reduces the heat flux to the centre of the crystal.

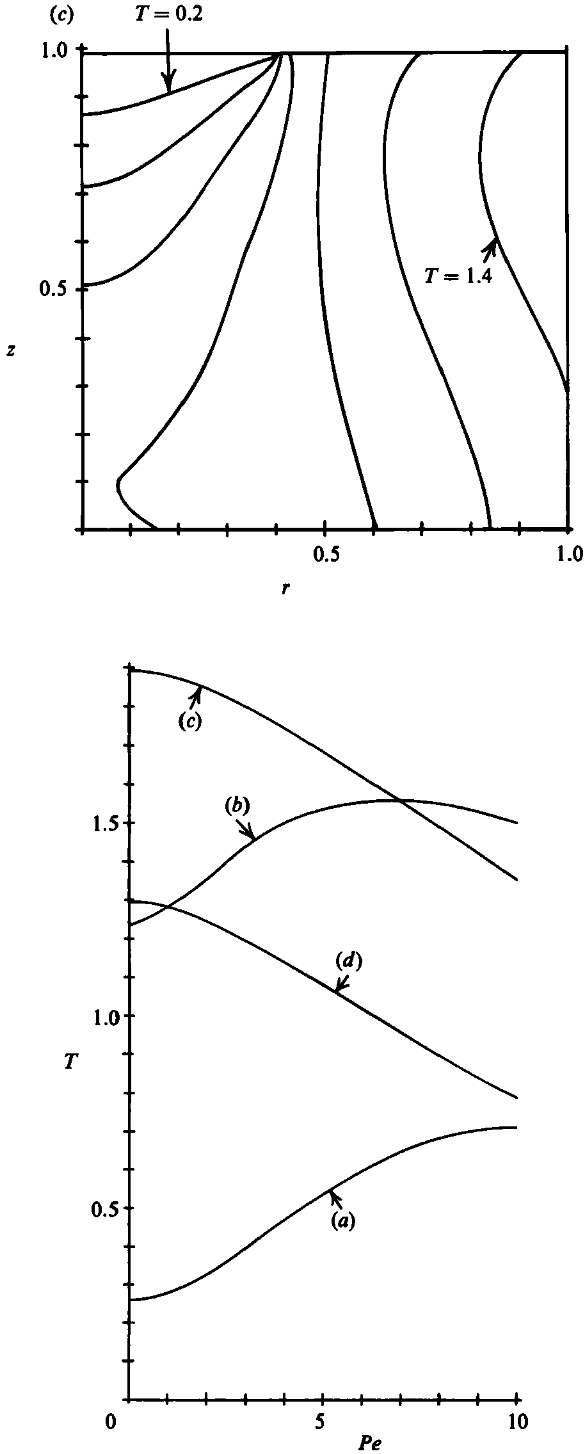

FIGURE 7. Temperatures for $b = 0.9875$, $C_0 = 0.66$ and $D_1 = -D_0 = 0.25$. (*a*) Isotherms for $Pe \ll 1$: $T = 0.2m$, for $m = 1$–9. (*b*) Isotherms for $Pe = 3$ ($B = 0.188$ T): $T = 0.2m$, for $m = 1$–8. (*c*) Isotherms for $Pe = 10$ ($B = 0.103$ T): $T = 0.2m$, for $m = 1$–7. (*d*) Temperatures for $Pe = 0$–10: (*a*) T at $r = a + 0.025$ and $z = b$, (*b*) T at $r = 1$ and $z = b$, (*c*) T at $r = 1$ and $z = 0$, and (*d*) T at $r = z = 0$.

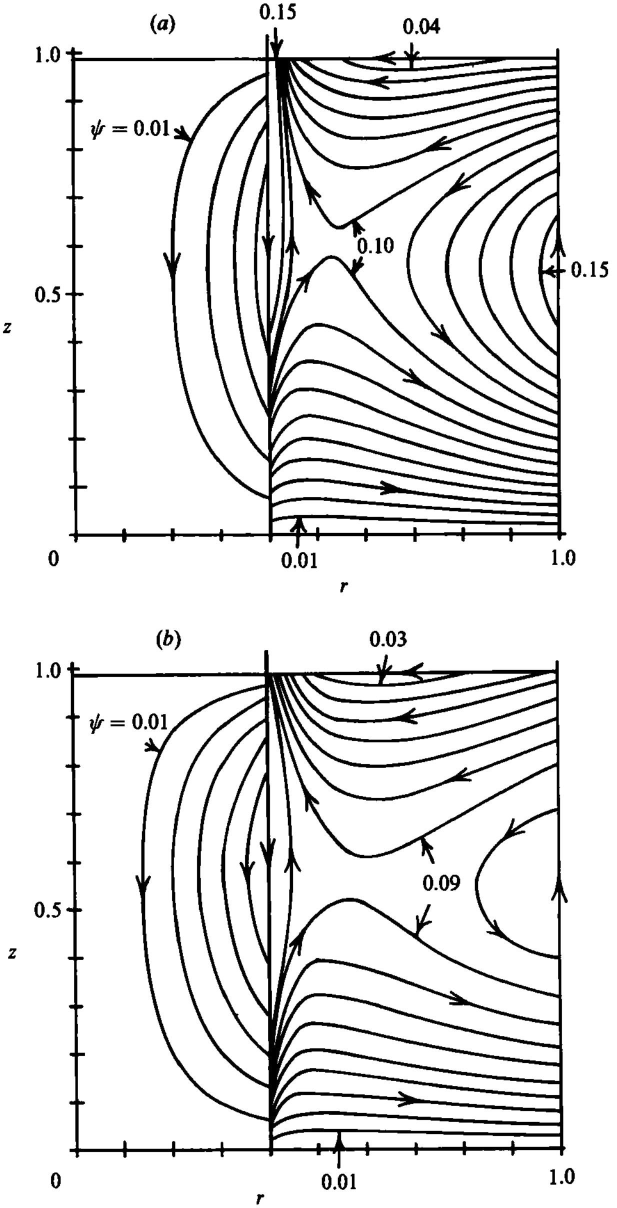

FIGURE 8. Streamlines for the melt motion due to both buoyancy and thermocapillarity with $b = 0.9875$, $C_0 = 0.66$ and $D_1 = -D_0 = 0.25$. (a) $Pe = 3$ and $\psi = 0.01m$, for $m = 1$–15. (b) $Pe = 10$ and $\psi = 0.01m$, for $m = 1$–10. Some of the streamlines near $r = a$ and $z = b$ are not shown. Upward flow inside the vertical wall layer, inward flow inside the free-surface Hartmann layer and downward flow inside the free-shear layer are represented by the lines at $r = 1$, $z = b$ and $r = a$, respectively.

The isotherms for $Pe = 0.5$ are virtually indistinguishable from those for $Pe \ll 1$. Therefore, the pure-thermal-conduction solution is certainly valid for $Pe \leqslant 0.5$ ($B \geqslant 0.461$ T). In fact, there are only slight differences between the isotherms for $Pe = 1$ and those for $Pe \ll 1$, so the pure-conduction solution is relatively accurate for $B \geqslant 0.326$ T.

The streamlines for $b = 0.9875$ and for $Pe = 3$ or 10 are presented in figure 8. The corresponding streamlines for $Pe \ll 1$ are presented in figure 6(*a*). While the isotherms for these three values of Pe are radically different, the streamlines are remarkably similar. This similarity is due primarily to two aspects of the normalization. First, the characteristic velocity U varies as B^{-2}, so that a given $\Delta\psi$ represents four times as much flow for $B = 0.1$ T as for $B = 0.2$ T. Secondly, U is proportional to (ΔT), which is defined as qL/k. While q may be different for different B, the dimensionless ψ is relatively insensitive to changes in B.

There are three significant variations of the streamlines with Pe. The first variation is that, as Pe increases from 0, the circulation at $r = 1$ first increases and then decreases. The stream function for the buoyancy-driven motion at $r = 1$ is given by (10*c*) with the jump condition (16) for the radial temperature gradient in the outer core at $r = 1$. For $Pe \ll 1$, $\partial T_0/\partial r = 1$ at $r = 1$ and the buoyancy ψ_0 is given by (18). As Pe increases from 0, the jump condition (16) indicates that $\partial T_0/\partial r$ at $r = 1$ is greater than 1 when $\partial T/\partial z < 0$ here. As long as the temperature at the free surface is less than that at the bottom, then the fluid flowing upward inside the vertical wall layer cools and rejects heat. The rejected heat augments the heat input to the vertical wall, so that the outer core receives a heat flux greater than q. The maximum value of ψ at $r = 1$ rises from 0.14 for $Pe \ll 1$ to 0.155 for $Pe = 3$. At $Pe = 7$, the free-surface and bottom temperatures at $r = 1$ are equal. For $Pe > 7$, the free surface is hotter than the bottom, so that the rising fluid inside the vertical wall layer must absorb heat. The heat flux into the outer core is less than q and the maximum value of ψ at $r = 1$ decreases to 0.11 for $Pe = 10$.

The second significant variation of the streamlines with Pe concerns the thermocapillary-driven flow, which is proportional to the value of $\partial T/\partial r$ at $z = b$. The curves (*a*) and (*b*) in figure 7(*d*) indicate that the temperature difference between $r = a+0.025$ and $r = 1$ at the free surface does not change significantly for $Pe = 0$–10, so that the free-surface temperature gradient and the thermocapillary-driven flow for $0.5 < r < 1$ does not change much as Pe increases. However, T at $r = a+0.025$ and $z = b$ increases by a factor of 2.75 as Pe increases from 0 to 10, so that the thermocapillary-driven circulation near $r = a$ increases greatly as Pe increases. The value of ψ_0 at $r = a$ and $z = b$ increases from 0.15 for $Pe \ll 1$, to 0.24 for $Pe = 3$ and then to 0.40 for $Pe = 10$. This strong, axially elongated, counterclockwise circulation near $r = a$ is actually nearly coincident with a strong, axially elongated, clockwise circulation inside the free-shear layer due to the differential rotation of the crystal and crucible (Hjellming & Walker 1986). This competition is not important for the thermal problem, as discussed in the next section. However, it is important for the mass transport problem.

The third important variation of the streamlines with Pe is the increase in the inner-core circulation as Pe increases. The isotherms in figure 7(*a*) indicate that there is little radial temperature gradient in the inner core for $Pe \ll 1$. As Pe increases, figure 7(*b*, *c*) indicates that the radial temperature gradients increase here, and (10*c*) indicates that the circulation increases. As mentioned above, the shift from the thermal conduction to convection leads to a concentration of the heat flux to the crystal near its edge and this concentration accounts for the increased slope of the isotherms in the inner core in figure 7(*c*).

7. Superposition of other melt motions

In a typical Czochralski process, the crystal and crucible are rotated about the axis of symmetry with different angular velocities. These rotations produce an azimuthal melt motion (v_θ), and the centrifugal force associated with v_θ drives an additional meridional motion (v_r and v_z). Hjellming & Walker (1986) treat the meridional motion due to the centrifugal force assuming that all inertial effects, except the radial centrifugal force v_θ^2/r, are negligible. To extend the present analysis to include the melt motions associated with the crystal and crucible rotations, we simply add the stream function for the melt motion due to the centrifugal force to those for the motions due to buoyancy (10*c*) and thermocapillarity (27*a*). This superposition is only justified when the magnetic field is sufficiently strong that all inertial effects are negligible, i.e. for $N \gg 1$. We use the total stream function in each core to determine the velocities for the left-hand side of the heat equation (2*e*). The numerical solution for $T(r, z)$ now depends on two new parameters: the ratio of the angular velocities of the crystal and crucible and the ratio of U to the characteristic velocity for centrifugal pumping,

$$U_{\mathrm{CF}} = \frac{\rho \Omega^2 L}{\sigma B^2},$$

where Ω is the crucible angular velocity. In the following paragraphs we show that the melt motion due to the centrifugal force has a negligible effect on the temperature for modest rotation rates, say 15–20 r.p.m. In this case, we can ignore the crystal and crucible rotations when we solve (2*e*) for the temperature, which determines the motions due to buoyancy and thermocapillarity. We then simply superimpose the melt motions due to the centrifugal force, buoyancy and thermocapillarity.

In the outer core, vertical wall layer, adjacent Hartmann layers and adjacent intersection regions, there is no melt motion driven by the centrifugal force. For $r > a$ the melt rotates as a rigid body with the crucible. The centrifugal force drives a very strong, clockwise, axially elongated circulation which is entirely inside the free-shear layer. However, the free-shear-layer stream function associated with this internal circulation goes to zero as $R \rightarrow \pm\infty$. Therefore the jump condition (31) shows that this circulation does not affect the radial heat flux through the free-shear layer. There is a downward flow inside the free-shear layer for $0 < R < \infty$ which is absorbing heat and becoming hotter, while there is an equal upward flow for $-\infty < R < 0$ which is rejecting an equal amount of heat and becoming cooler. Finally the centrifugal force drives a much weaker circulation through the inner core, free-shear layer and Hartmann layers on the crystal face and on the crucible bottom for $r < a$. This circulation decreases roughly like B^{-3}, as B is increased. The magnetic field produces a body force that opposes all melt circulations and that increases like B^2, as B is increased. The magnetic field does not significantly alter the buoyancy or thermocapillarity forces, so they drive circulations that decrease roughly like B^{-2}. The magnetic field makes the $O(1)$ inner core v_θ independent of z, so that its centrifugal force is balanced by a radial pressure gradient. Circulations are driven by the axial variation of v_θ that cannot be balanced by a radial pressure gradient. The axial variations of the $O(1)$ v_θ are confined to the Hartmann layers, while only the $O(M^{-1})$ inner core v_θ varies with z. Therefore the magnetic field alters the centrifugal force so that the difference between it and the radial pressure gradient decreases like B^{-1}, as B is increased.

The centrifugal force can produce clockwise or counterclockwise circulations, or both, in the inner core, and can produce either a net upward or downward flow inside the free-shear layer. We know how the melt motions due to buoyancy and thermocapillarity affect $T(r,z)$ for various values of Pe, corresponding to different magnetic-field strengths. If the upward or downward flow in the free-shear layer due to the centrifugal force is much smaller than the downward flow due to thermocapillarity and buoyancy, then the melt motion due to the centrifugal force has a negligible effect on $T(r,z)$. For thermocapillarity and buoyancy, the maximum value of the $\Delta\psi$ across the free-shear layer is 0.15 for $Pe \leqslant 0.5$ ($B \geqslant 0.46$ T) and is slightly higher for larger values of Pe. Hjellming & Walker (1986) present the stream functions for the melt motions due to the centrifugal force. To translate their values of $\Delta\psi$ for the net flow inside the free-shear layer into the present normalization, we multiply their values by

$$\frac{U_{\mathrm{CF}}\,a^2}{UM} = 6.875\Omega^2a^2M^{-1}.$$

If the crucible and crystal are rotating in opposite directions at 1.57 rad/s (15 r.p.m.), then the maximum values of $\Delta\psi$ for the net axial flow inside the free-shear layer due to the centrifugal force are 0.0062, 0.0044, 0.0034, 0.0028, 0.0020 and 0.0014 for $Pe = 10, 5, 3, 2, 1$ and 0.5, respectively. Clearly these values are negligible compared with 0.15 and would still be negligible for considerably larger rotation rates. The melt motions associated with the crystal and crucible rotations involve relatively large radial velocities in the Hartmann layers on the crystal face and on the crucible bottom for $r < a$. These jets have a negligible effect on the temperature because these layers are in relatively isothermal regions (see figure 7). However, these jets strongly affect the transport of oxygen from the crucible bottom for $r < a$ and the transport of oxygen or dopants to the crystal face. Therefore the flows due to centrifugal pumping can generally be ignored in determining the thermally driven motions, but are very important for the mass transport.

In a typical Czochralski process, the crystal grows at a rate of 0.025 mm/s, and the crucible is raised at a rate of 0.004 mm/s in order to keep the free surface at the same elevation. For an unsteady flow, we would introduce a time derivative into the operator D in (2a, b, e). However, the pull velocity (rate of crystal growth) is so small that it is appropriate to neglect this transient term and to treat the melt motion as an instantaneous, steady flow. In addition to the instantaneous motions due to the centrifugal force, buoyancy and thermocapillarity, we have the instantaneous melt motion due to the crystal growth. We solve (2a–c) without the inertial and buoyancy terms. We normalize the velocities with the pull velocity, so that the boundary conditions are

$$v_r = 0, \quad v_z = 1 \quad \text{at } z = b \quad \text{for } 0 < r < a, \qquad (32a,b)$$

$$\frac{\partial v_r}{\partial z} = 0, \quad v_z = 0 \quad \text{at } z = b \quad \text{for } a < r < 1, \qquad (33a,b)$$

$$v_r = v_z = 0 \quad \text{at } r = 1, \qquad (34a,b)$$

$$v_r = 0, \quad v_z = a^2 \quad \text{at } z = 0. \qquad (35a,b)$$

The Hartmann layers match any radial core velocities and satisfy the conditions (32a), (33a), (35a). The vertical wall layer matches any axial outer-core velocity, satisfies the condition (34b), and does not involve any large velocities. The free-shear layer matches a jump between the inner- and outer-core axial velocities and does not involve any large velocities. With the stream function again defined by (10a, b), the inner- and outer-core stream functions for the instantaneous melt motion associated with the crystal growth are

$$\psi_\mathrm{i} = \frac{1}{2b}[a^2b(1-r^2)-(1-a^2)\,r^2z], \tag{36a}$$

$$\psi_\mathrm{o} = \frac{a^2}{2b}(b-z)(1-r^2). \tag{36b}$$

The thermal convection associated with this melt motion is negligible, but the mass transport, particularly from the outer to inner cores and from the inner core to the crystal, is important. The values (36) must be multiplied by the ratio of U to the pull velocity before being added to the other stream functions (10*c*), (27*a*).

8. Conclusions

The heat leaving the melt at the crystal face, plus the heat released during crystallization, equals the heat lost by the crystal due to radiation and due to conduction to the argon gas. This balance determines the crystal growth rate. In a Czochralski puller, the electric current to the heater is varied during the growth of a crystal in order to achieve a constant growth rate. Therefore the heat leaving the melt at the crystal face is a key variable in the process control. The dimensional total heat transfer rate from the melt at the crystal face is $Q_\mathrm{s}\,qL^2$, where the dimensionless heat transfer rate Q_s is given in table 2 for each case considered here. Since temperatures and heat losses for the crystal surface have been studied both experimentally and numerically, reasonably accurate estimates of the heat transfer rate from the melt at the crystal face, for a given growth rate and for a given stage in the growth of the crystal, might be possible. The values of Q_s in table 2 then give the values of q and ΔT to be used in the non-dimensionalization. The heat flux at the vertical crucible wall, q, should still be used to define the dimensionless variables because this gives the boundary condition (7*c*), which leads to dimensionless stream functions that are relatively insensitive to changes in several parameters.

The dimensionless heat transfer rate into the melt at the vertical crucible wall is $2\pi b = 6.20$, 3.06 and 1.49 for $b = 0.9875$, 0.4875 and 0.2375, respectively. The ratio of Q_s to one of these values gives the fraction of the heat entering at $r = 1$ that reaches the crystal face. Cases 1–3 in table 2 involve changes in C_0 for constant b and Pe. As C_0 increases, more heat is lost through the free surface, so that less reaches the crystal. Cases 4–6 involve changes in b for constant Pe and with C_0 from the radiation calculation. As b decreases, there is less heat input at the vertical crucible wall, but more through the bottom. Cases 4 and 7–16 involve changes in Pe (or B) for constant b and C_0. The variation here follows curve 2 in figure 7(*d*). As Pe increases from zero (B decreases from ∞), the free surface gets hotter and loses more heat, so that less heat reaches the crystal. However, as Pe passes 7, the free-surface temperature begins to drop, so that Q_s increases slightly.

The present analysis assumes that the axial magnetic field is sufficiently strong that the inertial terms on the left-hand sides of (2*a*, *b*) are negligible everywhere and that the viscous terms are only significant in the boundary and free-shear layers. For the isothermal melt motion driven by the crystal and crucible rotations, Hjellming & Walker (1986) conclude that this assumption is invalid for $B \leqslant 0.05$ T, is valid for $B \geqslant 0.2$ T and gives qualitatively correct results for $B = 0.1$ T. Comparison of the present predictions and the results of numerical analyses, which include inertial and viscous effects everywhere, leads to the same conclusion for the buoyant and

Case	C_0	Pe	Q_s
1	0	0	3.99
2	0.5	0	3.12
3	1	0	2.26
4	0.66	0	2.85
5	0.232	0	1.86
6	0.101	0	1.14
7	0.66	1	2.79
8	0.66	2	2.73
9	0.66	3	2.61
10	0.66	4	2.54
11	0.66	5	2.48
12	0.66	6	2.44
13	0.66	7	2.42
14	0.66	8	2.42
15	0.66	9	2.43
16	0.66	10	2.46

TABLE 2. Dimensionless heat transfer rate from the melt at the crystal face Q_s. $C_1 = 0.493$ and $a = 0.4$ for every case; $b = 0.9875$ and $D_1 = -D_0 = 0.25$ for every case except for case 5 ($b = 0.4875$, $D_0 = 0$ and $D_1 = 0.25$) and case 6 ($b = 0.2375$, $D_0 = 0$ and $D_1 = 0.5$).

thermocapillary convections. Langlois & Lee (1983*b*) present streamlines for the melt motions without rotation of the crystal or crucible, with the present values of α and $\mathrm{d}\gamma/\mathrm{d}T^*$, with $b = 0.66$, and with $B = 0, 0.05$ or 0.1 T. For $B = 0$, the flow is primarily a buoyant convection which fills the entire melt. There is some thermocapillary pumping over the entire free surface, so that the first streamline is closer to the free surface than it is to the bottom. The only effect of the large free-surface temperature gradient at $r = a$ is that two of the twenty-two streamlines are pulled to the crystal edge by thermocapillarity. However, this is a very local effect near the crystal edge. For $b = 0.05$ T, the magnetic field is beginning to prevent penetration of the circulation into the region under the crystal. The concentration of the upward flow into the vertical wall layer is evident. The thermocapillary acceleration of the flow due to the large free-surface temperature gradient affects every streamline near $r = a$. This acceleration produces a jet near the crystal edge and this jet is carried by inertia to $r = 0.5a$, so that inertial effects are still important. For $B = 0.1$ T, the outer-core convection does not penetrate inside $r = 0.8a$. This suggests that the free-shear layer has emerged and has a thickness of $0.2a = 0.08$, which is comparable to $M^{-\frac{1}{2}} = 0.05$ for this B. The strong, axially elongated thermocapillary convection at $r = a$ is clearly visible. The flow executes abrupt 90° turns near the crystal edge, indicating that the electromagnetic body force overwhelms the inertial 'force'. For this case, we conclude that the present analysis is probably reasonably accurate for $B \geqslant 0.1$ T, with the accuracy improving as B increases.

Langlois & Lee (1983*b*) also present results for the same conditions, except that $\alpha = 1.41 \times 10^{-4}\ \mathrm{K}^{-1}$, i.e. ten times the value used here and the value for their 'low-buoyancy' case. In the present analysis, there would be two effects of increasing the value of α (Hjellming & Walker 1987). First the value of B that would correspond to a given value of N or Pe increases. For a ten-fold increase in α, the values of B in table 1 must be multiplied by 1.78 or 3.16 to obtain the same value of N or Pe, respectively. Here we are concerned with the minimum B for which the inertialess analysis applies, so that we would expect this minimum B to increase by a factor of 1.78. The high-buoyancy results of Langlois & Lee (1983*b*) for $B = 0.1$ or 0.2 T correspond very closely to their low-buoyancy results for $B = 0.05$ or 0.1 T, respectively. For the high-buoyancy case, we conclude that the present inertialess approach is reasonably accurate for $B \geqslant 0.2$ T. Kim & Langlois (1986) use a temperature difference between the crystal and crucible of $\Delta T = 18$ K, rather than the 100 K used in table 1 here or the 88 K used by Langlois & Lee (1983*b*). If the characteristic temperature difference is actually this small, then the $\alpha(\Delta T)$ for high buoyancy is only 1.8 times that used here, so that the values of B in table 1 need only be multiplied by 1.16 or 1.34 for the same N or Pe, respectively.

The second effect of changing α is to change Q. With α multiplied by ten, Q is multiplied by 0.1, and the thermocapillary stream function (27*a*) is multiplied by 0.1 before being added to the buoyancy stream function (10*c*). For $b = 0.9875$ and $Pe \ll 1$, this would eliminate the axially elongated thermocapillary convection at $r = a$ (Hjellming & Walker 1987). However, the high-buoyancy results of Langlois & Lee (1983*b*) for $B = 0.2$ T clearly exhibit an axially elongated thermocapillary convection at $r = a$, which is a third of the total flow. For their case, $b = 0.66$ and $Pe = 27$. As b is reduced from 0.9875 to 0.66, the buoyancy circulation is reduced by a factor of 0.45, while the thermocapillary convection remains essentially unchanged. As Pe increases from 0 to 10, curve 1 in figure 7(*d*) indicates that the free-surface temperature gradient at $r = a$ increases by a factor of nearly three. Since this curve has levelled off by $Pe = 10$, we can expect a comparable factor at $Pe = 27$. Therefore, relative to figure 6(*a*), if we reduce Q by a factor of 0.1, reduce b from 0.9875 to 0.66 and increase Pe from 0 to 27, then the ratio of the thermocapillary to buoyant convections has only been reduced by 33%, and we would still expect an axially elongated thermocapillary convection at $r = a$.

The concentration $C(r, z)$ of oxygen or of a dopant such as boron is governed by (2*e*) with T replaced by C and with Pe replaced by Pe_{m}, which is the Péclet number for mass transport. This mass Péclet number is given by the definition of Pe with the thermal diffusivity $(k/\rho c_h)$ replaced by the appropriate diffusion coefficient. The diffusion coefficient for oxygen or boron in silicon is 8×10^{-4} or 2.4×10^{-3} times the thermal diffusivity of silicon, respectively (Lee, Langlois & Kim 1984; Kim & Langlois 1986). When the Péclet numbers in table 1 are divided by either of these factors, the resultant values of Pe_{m} are very large. Therefore, asymptotic solutions for $Pe_{\mathrm{m}} \gg 1$ are appropriate, and diffusion is negligible outside the boundary and free-shear layers. Oxygen enters the melt from the crucible and either evaporates from the free surface or is incorporated into the crystal. Without a magnetic field, convective velocities which are much larger than the present U and turbulence effectively mix the melt, so that there is never a large concentration variation in the melt. Without turbulence and with magnetically suppressed convection, large concentration variations can develop in a magnetic Czochralski puller. The present solutions indicate some of the factors that affect these concentration variations.

None of the $O(1)$ flow enters the Hartmann layer on the crucible bottom for $a \leqslant r \leqslant 1$, and this layer merely matches the radial velocity due to buoyancy and thermocapillarity. Since diffusion is confined to boundary layers, the oxygen from the crucible bottom cannot reach the main $O(1)$ flow in the outer core. Therefore the oxygen concentration in the Hartmann layer builds up to the saturation point, and no more oxygen enters the melt from the bottom. This conclusion is confirmed by experiments which show that a light-brown layer of silicon oxides develops on the crucible bottom with a strong axial magnetic field. No such layer occurs without a magnetic field.

All the buoyant convection and part of the thermocapillary convection flow vertically upward inside the vertical wall layer at $r = 1$. The high-velocity flow inside this layer sweeps away the entering oxygen before its concentration builds up. Therefore the melt dissolves the vertical crucible wall throughout the growth of a crystal. This conclusion is also confirmed by the same experiments which show that the vertical crucible wall remains clean and is rather deeply eroded at the end of the process.

The oxygen that does not evaporate from the free surface enters the crystal so that the evaporation rate is very important. With only buoyancy, none of the $O(1)$ flow enters the free-surface Hartmann layer, so that an oxygen-depleted layer would develop here and evaporation would effectively cease. The thermocapillary convection pulls part of the flow from the vertical wall layer into the free-surface Hartmann layer, where it can lose much of its oxygen by evaporation. The balance between buoyant and thermocapillary convection is clearly important in determining the fraction of the oxygen that evaporates. In figure 6(*a*) for $Pe \ll 1$, every streamline that enters the inner core beneath the crystal face has traversed the entire free surface, so that we would expect a low oxygen concentration as this flow enters the inner core. In figure 8(*b*) for $Pe = 10$, half of the flow entering the inner core has traversed the entire free surface, while the other half has only been inside the free-surface Hartmann layer for $0.4 < r < 0.5$. If α is in fact ten times the value used here, then the fraction of the thermally driven motion entering the free-surface Hartmann layer and losing oxygen by evaporation is greatly reduced (Hjellming & Walker 1987).

Mass transport in the free-shear layer is very complex. There are three superposed flows here: (i) the elongated, counterclockwise thermocapillary circulation located on the outer side of the free-shear layer, (ii) the elongated, clockwise circulation due to centrifugal pumping and located on the inner side of the free-shear layer, and (iii) the uniform inward flow due to crystal growth. The competition of the two elongated circulations is demonstrated by the numerical results presented by Langlois, Hjellming & Walker (1987), who do not include crystal-growth effects, but do include inertial and viscous effects. As a fluid element moves from the outer to inner cores, it is first swept upward to the free surface near the crystal edge, it is then swept downward to the crucible bottom at $r = a$, and finally is swept up to the crystal face near $r = a$. The rising and falling columns of fluid are sufficiently close for significant diffusion between them. As the fluid element approaches the crystal face, it may move inward inside the crystal-face boundary layer and be incorporated into the crystal, or it may move into the central part of the inner core. This depends on the rotation rates of the crystal and crucible (Hjellming & Walker 1986). The analysis of the mass-transport problems based on the present solutions for the melt motions will be presented in a future paper.

This research was supported by the US National Science Foundation under Grant CBT-8519976. Valuable information about the Czochralski process has been provided by W. E. Langlois of the IBM Almaden Research Center and by J. P. DeLuca, R. A. Frederick and J. W. Moody of the Monsanto Electronic Materials Company. The Sigma Xi society provided a Grant-in-Aid for travel related to this research. Four reviewers suggested ways to clarify the presentation of this research.

REFERENCES

HJELLMING, L. N. & WALKER, J. S. 1986 Melt motion in a Czochralski crystal puller with an axial magnetic field: isothermal motion. *J. Fluid Mech.* **164**, 237–273.

HJELLMING, L. N. & WALKER, J. S. 1987 Melt motion in a Czochralski crystal puller with an axial magnetic field: uncertainty in the thermal constants. Submitted to *J. Cryst Growth.*

KIM, K. M. & LANGLOIS, W. E. 1986 Computer simulation of boron transport in magnetic Czochralski growth of silicon. *J. Electrochem. Soc.* **133**, 2586–2590.

KURODA, E., KOZUKA, H. & TAKANO, Y. 1984 The effect of temperature oscillations at the growth interface on crystal perfection. *J. Cryst. Growth* **68**, 613–623.

LANGLOIS, W. E. 1981 Convection in Czochralski growth melts. *Physico chem. Hydrodyn.* **2**, 245–261.

LANGLOIS, W. E., HJELLMING, L. N. & WALKER, J. S. 1987 Effects of the finite electrical conductivity of the crystal on hydromagnetic Czochralski flow. Submitted to *J. Cryst Growth.*

LANGLOIS, W. E. & KIM, K. M. 1987 The effect of incorporating radiation enclosure theory into the simulation of melt flow in magnetic Czochralski growth of silicon. In *Proc. 2nd ASME/JSME Thermal Engng Joint Conf., Honolulu, March, 1987.*

LANGLOIS, W. E. & LEE, K. J. 1983*a* Czochralski crystal growth in an axial magnetic field: effects of Joule heating. *J. Cryst. Growth* **62**, 481–486.

LANGLOIS, W. E. & LEE, K. J. 1983*b* Digital simulation of magnetic Czochralski flow under various laboratory conditions for silicon growth. *IBM J. Res. Develop.* **27**, 281–284.

LANGLOIS, W. E. & WALKER, J. S. 1982 Czochralski crystal growth in an axial magnetic field. In *Computational and Asymptotic Methods for Boundary and Interior Layers, Proc. BAIL II Conf.*, pp. 299–304.

LEE, K. J., LANGLOIS, W. E. & KIM, K. M. 1984 Digital simulation of oxygen transfer and oxygen segregation in magnetic Czochralski growth of silicon. *Physico Chem. Hydrodyn.* **5**, 135–141.

RAMACHANDRAN, P. A. & DUDUKOVIC, M. P. 1985 Simulation of temperature distribution in crystals grown by Czochralski method. *J. Cryst. Growth* **71**, 399–408.

SRIVASTAVA, R. K., RAMACHANDRAN, P. A. & DUDUKOVIC, M. P. 1985 Interface shape in Czochralski grown crystals: effect of conduction and radiation. *J. Cryst. Growth* **73**, 487–504.

SRIVASTAVA, R. K., RAMACHANDRAN, P. A. & DUDUKOVIC, M. P. 1986 Radiation view factors in Czochralski crystal growth apparatus for short crystals. *J. Cryst. Growth* **74**, 281–291.

STERN, E. J. 1985 Mathematical modelling of radiative heat exchanges in Czochralski crystal pulling. *IMA J. Appl. Maths* **35**, 205–222.

WALKER, J. S., LUDFORD, G. S. S. & HUNT, J. C. R. 1971 Three-dimensional MHD duct flows with strong transverse magnetic fields. Part 2. Variable-area rectangular ducts with conducting sides. *J. Fluid Mech.* **46**, 657–684.